PAPER • **OPEN ACCESS**

Custom FDM-based bioprinter with heated nozzle: optimizing slicer settings for precision printing using a print quality index

To cite this article: Leif O Meyer *et al* 2025 *Biomed. Mater.* **20** 035030

IOP Publishing Biomed. Mater. 20 (2025) 035030 https://doi.org/10.1088/1748-605X/add230

Biomedical Materials

OPEN ACCESS

RECEIVED
11 October 2024

REVISED
2 April 2025

ACCEPTED FOR PUBLICATION
29 April 2025

PUBLISHED
9 May 2025

PAPER

Custom FDM-based bioprinter with heated nozzle: optimizing slicer settings for precision printing using a print quality index

Leif O Meyer, Valérie Jérôme and Ruth Freitag*

Process Biotechnology, University of Bayreuth, Germany
* Author to whom any correspondence should be addressed.

E-mail: ruth.freitag@uni-bayreuth.de and valerie.jerome@uni-bayreuth.de

Keywords: custom bioprinter, thermal gelation, slicer optimization, print quality

Supplementary material for this article is available online

Abstract

Bioprinting of microtissues has become a standard technique in medical and biotechnological research, offering a more accurate replication of the *in vivo* setting than conventional 2D cell culture. However, widespread adoption is limited by the absence of a universally accepted printing benchmark—common in standard fused deposition modeling (FDM) printing, as well as the high cost and restricted customizability of commercial bioprinters. This study introduces a method to convert a standard FDM printer into a bioprinter. All cell-contacting components are biocompatible and autoclavable, while the printer body can be UV-sanitized. Using a heated FDM printhead, we used the thermal properties of alginate-gelatin bioinks to achieve high-resolution 3D printing. A key achievement was the developed print quality index (PQI) method, which correlates nozzle temperature with bioink flow behavior, streamlining optimization of slicer settings. Guided by PQI, we reproducibly bioprinted complex alginate-gelatin structures with high quality and dimensional/geometric accuracy. A case study using recombinant HuH7^{EGFP} cell-laden hydrogels demonstrated long-term cell proliferation, confirming high viability. Given its efficiency, the PQI method has the potential to become the missing printing benchmark for slicer optimization in bioprinting. The presented approach significantly advances the accessibility of sophisticated bioprinting technology to interested research groups worldwide.

1. Introduction

By creating 3D tissue-like structures, bioprinting has the potential to advance the development of new therapies and treatments [1, 2]. Recent progress in the field has enabled researchers to design increasingly complex and functional cellular assemblies, with applications ranging from repairing neural tissue and spinal cords [3] to engineering bone and dental [4, 5] as well as hepatic [6] and cardiac [7] tissues. This potential has attracted companies to invest in the development of commercial bioprinters [8]. However, the currently available commercial bioprinters share drawbacks, like high costs to obtain and operate, while proprietary bioink formulations often limit flexibility. Furthermore, the devices and their operating software are typically not open-sourced, which can further restrict applications. Bioprinters developed by academic researchers, on the other hand, frequently focus on establishing or advancing state-of-the-art methodologies (e.g. coaxial extrusion [9], multi-axis support [10]). As a result, many published bioprinters tend to be complex and highly specialized [9, 11–17].

In addition, several groups have proposed simple and easy-to-implement approaches as entry points for bioprinting [18–23]. In such cases, regular 3D printers, e.g. those intended for polymer filaments, are typically used as a starting point. For example, *Alvarez'* research group took a standard fused deposition modeling (FDM) printer and substituted the extruder with their proprietary design [20]. An external syringe pump was employed to extrude bioink through a custom-designed print head. The latter was equipped with an external water cooling system to enable temperature regulation, facilitating bioprinting at various nozzle temperatures. However, their setup required three systems

to operate simultaneously: Gcode controlling the printer head movement, the external syringe pump managing material extrusion, and the water cooling/heating loop regulating the nozzle temperature. While this system proved effective in bioprinting experiments, it was limited in its ability to produce structures with the height and geometric complexity required for specific medical applications [20]. One potential reason for this limitation is the system's division into independently operated subsystems, which may have hindered the synchronization of their operational task. This synchronization of tasks (i.e. movement, material extrusion, etc) is crucial for 3D printing and is typically managed by the slicing software (also referred to as slicer) in commercial printers. *Gilbert*'s group developed an FDM-based bioprinter capable of producing structures exceeding 10 mm in height and allowing high repeatability using highly viscous 5 wt.% alginate/5 wt.% gelatin hydrogels [19]. To achieve this, they integrated a syringe pump into the print head, utilizing a plastic syringe as the bioink reservoir and a sterile cannula as the nozzle. This approach allowed them to utilize the existing extruder motor and software, enabling the machine to be operated like a traditional FDM printer with any open-source slicer. However, this bioprinter suffered from significant dimensional inaccuracies in the printed structures (compared to the targeted dimensions) due to a combination of mechanical shortcomings. These include the deformation of some flexible plastic-based components (e.g. the syringe holding unit), slipping of warehouse-quality threaded rods, and inconsistent pressure from the plastic syringe and plunger during hydrogel extrusion.

The slicing software plays a fundamental role in regular 3D printing by translating geometric data from computer-aided design (CAD) software into specific commands for the printer. It also optimizes the print behavior according to the specific geometry [16, 24]. To achieve accurate geometric results, the amount of extruded material must be precisely controlled to match the set layer height, ensuring consistent nozzle-to-print distance throughout the print. Critical slicer settings (i.e. nozzle and print bed temperature, cooling fan operation, retraction properties, print speed, layer height) must be carefully adjusted for each material, as they significantly impact printing performance. Among these, the nozzle temperature is the most frequently adjusted parameter due to its dominant influence on the viscosity of the polymer filament. If the filament is too viscous, the layer-to-layer adhesion is weakened, making the structure prone to breakage or delamination. Conversely, if the filament is too hot and hence not viscous enough, it may drip unintentionally from the nozzle, causing stringing artifacts. Issues like these can be counteracted with retraction and coasting. Retraction involves a slight withdrawal of the filament between nozzle activations, while coasting stops extrusion slightly before the nozzle is deactivated, allowing built-up pressure to dissipate. Inadequate cooling can further exacerbate these issues, allowing the filament to remain molten for too long after extrusion, which can lead to flow effects post-extrusion that compromise structural accuracy [16]. Even though bioprinting and plastic FDM printing both involve controlling the flow of material on the print bed and previous layers, the aspect of setting the slicing parameters is largely neglected in the pertinent literature on bioprinting. This may stem from the widespread use of in-house-made hydrogels by research groups, which results in bioinks with diverse rheological properties [25]. These variations lead to different print behaviors, making adopting slicer settings from different groups challenging [26]. For example, the above-mentioned work from *Gilbert*'s group only partly reported on the optimization of the slicer settings parameters [19]. Given the similarities in the fundamental challenges of printing 3D geometries between traditional FDM printing and FDM-based bioprinting, it is reasonable to assume that optimizing slicer parameters could improve print quality in bioprinting as well. However, the absence of a universally accepted printing benchmark—common in standard FDM printing—hinders progress in refining print quality.

Preserving high cellular viability during bioprinting experiments is another challenge. Besides printing temperature, the most influential parameters concerning viability are the bioink's viscosity, the nozzle diameter, and print speed, all of which determine the amount of shear force exerted on the bioink during extrusion. Reducing the viscosity reduces shear forces and increases cellular viability [27]. This can be achieved by exploiting thixotropic or shear-thinning effects through the hydrogel's formulation [28], thereby temporarily reducing the hydrogel's viscosity during printing. One of the most frequently employed hydrogels in bioprinting is a blend of alginate and gelatin. Alginate is shear thinning and is used mainly for its biocompatible crosslinking properties [29]. Gelatin is thermosensitive and melts at around 28 °C into a Newtonian fluid [30, 31]. The temperature dependency of the rheologic properties of alginate and gelatin-based hydrogels in bioprinting was first investigated by Ouyang *et al* [32]. These authors proposed a mathematical model to determine the appropriate extrusion temperature regarding possible under-, proper-, and over-gelation. They showed that different rheologic properties in the hydrogel can be obtained by adjusting the alginate vs. gelatin concentrations and that the ideal extrusion temperature for high geometric quality varies accordingly. Additionally, He *et al* [33] described the issue of parasitic flows on the print bed, a common

challenge in bioprinting. These challenges are comparable to those previously encountered in standard FDM printing, which were overcome by fine-tuning slicer software parameters using a universally accepted printing benchmark. Similarly, optimizing slicer settings is essential for improving bioprinting quality. However, unlike conventional FDM printing, slicer optimization in bioprinting not only influences print quality but also cell viability. Parameters such as extrusion temperature, print speed, volumetric flow rate, and cooling rate—among others—must be carefully adjusted to minimize mechanical and environmental stress on the cells during the printing process. Whereas printing bioink with higher viscosity allows for higher geometric fidelity, this exposes the cells to increased detrimental shear forces resulting in lower cell survival [34].

In this context, bioprinter development (i.e. hardware development) and slicer optimization (i.e. print parameter tuning) should be considered together to maximize the chance of success. For instance, the mechanical design must accommodate requirements for sterility and bioink rheology, while the bioink itself must balance printability with the ability to support cellular proliferation. These factors have to work seamlessly with the slicer settings, which need to be fine-tuned to achieve both reliable print performance and cell viability. This inherent complexity likely contributes to the absence of a universally accepted printing benchmark, unlike in standard FDM printing. Finding a delicate balance between print quality and cell viability during and after printing remains a significant challenge, often relying on a trial-and-error approach [35].

This study aims to establish a much-needed printing benchmark for bioprinting, similar to those used in FDM printing. Such a benchmark would facilitate the rapid identification of optimal slicer settings for high-quality hydrogel prints, minimizing dependence on time-consuming trial-and-error methods while providing a practical alternative to rheological analysis. Building on the work of Ouyang *et al* [32], who investigated the printability of alginate/gelatin-based hydrogels, we significantly enhanced the accuracy of their print-based evaluation method. Our refined approach enables precise determination of the optimal extrusion temperature for various alginate/-gelatin hydrogel compositions while providing valuable insights into the reproducibility of print quality.

First, we developed a bioprinter based on the design by Kahl *et al* [19], incorporating several modifications to enhance print quality. Specifically, we reworked the extruder for melt extrusion of alginate/gelatin-based hydrogels and refined the bioink formulation to optimize flow characteristics on the print bed. Alginate/gelatin was selected as a model thermosensitive bioink due to its widespread use in academic bioprinting labs, cost-effectiveness, reliable performance, and well-documented cell compatibility [36]. Furthermore, we examined the impact of different alginate/gelatin hydrogel compositions on cellular growth using recombinant human epithelial liver cancer cells ($HuH7^{EGFP}$), which express enhanced green fluorescent protein (EGFP) as model cells. This enabled us to assess how bioink modifications affect cellular survival and proliferation. Finally, we validated the integration of these pre-optimized experimental configurations through a conclusive bioprinting case study using the same cell line. By combining hardware adaptations, slicer optimizations, and a print-based evaluation method, this work establishes a practical framework for improving bioprinting reproducibility and biological performance.

2. Results and discussion

2.1. Design criteria for the conversion of a standard 3D printer to a bioprinter

The lack of a universally accepted printing benchmark makes optimizing slicer parameters in bioprinting challenging, often relying on trial and error. To address this, one of the goals of this work was to develop such a benchmark. To reach this goal, we aimed to produce both simple structures (i.e. two-layer grids) and more complex 3D ones with infill lines (i.e. reinforcing lines that cross the inside of a cylinder's outer wall, figure 1), which should serve for the evaluation of the printing performances. To support nutrient diffusion into the printed material, where cells will eventually reside, we designed these structures with line thicknesses of less than 500 µm, requiring high geometric precision during printing.

First, we adapted a commercially available FDM printer for bioprinting, following the approach described by Kahl *et al* [19]. This printer has a compact design, enabling its operation within a biosafety cabinet, which allows bioprinting under aseptic conditions. We initiated our work by replicating the 3D-printable extruder design made from polylactic acid (PLA) filament, which is referred to as 'Extruder I' (figure 2(A)). To ensure sterility during subsequent bioprinting experiments, all components that came into contact with cells were autoclavable or sterilized single-use parts. The entire system could be sterilized with UV irradiation within the biosafety cabinet.

During initial testing, we empirically determined applicable hydrogel compositions and slicer settings by fabricating simple geometries, such as straight lines (single and stacked layers), 90° bends, and when mentioned small cylinders, while experimenting with hydrogel formulations containing up to 20 wt. % gelatin and up to 10 wt. % alginate, both in phosphate-buffered saline (DPBS). The components alginate and gelatin were selected because (i) they are among the most widely used in academic

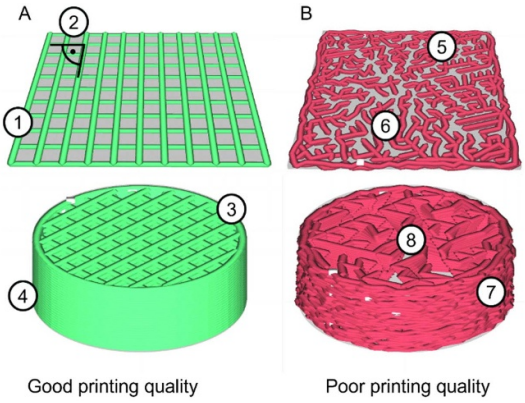

Figure 1. Evaluation of bioprinting performance (A) Anticipated bioprinting geometry (i.e. corresponding to geometric data from CAD software): a high-quality print exhibits consistent line widths (1), sharp and well-defined corners (2), and a smooth top layer with no gaps or collapses (3). The outer walls are straight and uniformly smooth, indicating precise layer stacking (4). (B) Poor printing performance (i.e. corresponding to putative printed structures): common defects include incomplete infill coverage with disconnected or irregularly spaced lines (5), inconsistent extrusion widths leading to uneven line thickness (6), and misaligned layers resulting in rough outer wall textures (7). Warping and collapsed layers, visible as deformed edges and sagging walls (8), further deviate from the intended geometry.

bioprinting labs and (ii) have been successfully used by Kahl *et al* in their customized FDM bioprinter. Alginate provides structural stability through ionic crosslinking, while gelatin enhances cell adhesion and mimics the extracellular matrix [19, 36, 37]. Before printing, the hydrogel components were thoroughly mixed and maintained at 45 °C for 60 min. Although gelatin typically melts around 28 °C, a higher temperature (45 °C) was chosen to ensure complete liquefaction and eliminate any residual thermal history of the polymers. The ranges of parameters tested are summarized in table 1. Post-printing the structures were qualitatively evaluated for print quality. Hydrogel composition and slicer settings were considered suitable for printing when the printed structures met the following quality criteria (QC): (QC1) line stability—printed lines maintained their shape without significant flattening on the print bed; (QC2) corner precision—corners remained sharp, avoiding rounding from material flow; (QC3) layer integrity—three stacked layers remained uniform, free from drops or dents; and (QC4) nozzle on/off accuracy—material extrusion began and stopped precisely as intended.

We initially adopted PLA filament slicer settings with a 0.2 mm layer height and a nozzle temperature of 25 °C, as the 'Extruder I' prototype was not capable of heating. Hydrogel formulations containing 0%–20% wt. gelatin and 0%–10% wt. alginate were tested by varying each component in 1% increments to assess the impact of different component ratios. 'Extruder I' successfully printed lines that did not flatten on the print bed, regardless of the hydrogel formulations and slicer setting parameters (i.e. meeting QC1). However, corners were rounded (i.e. failing QC2) and layers could not be reliably stacked to produce complex structures (i.e. failing QC3) (figure 2(A)). This was due to material flow post-extrusion resulting in irregularities. In terms of printable bioink, hydrogels containing 12%–14% gelatin alone performed the best, according to our acceptance criteria. However, as the syringe body was not temperature-controlled, the hydrogel was extruded in its gelled state at room temperature. The primary issue identified was faulty material extrusion caused by the extruder bending while applying force to the syringe due to the high viscosity of the hydrogel. This resulted in the hydrogel flow through the nozzle acting like being coupled to a spring. Hydrogel extrusion initiation was delayed as the spring accumulated deformation energy. Conversely, after the extruder motor halted, the hydrogel flow continued due to the release of stored deformation energy from the 'spring.' This unintended extrusion of hydrogel resulted in droplet formation on the print surface if the extruder did not move away promptly (i.e. failing QC4). A schematic illustrating this phenomenon in greater detail is provided in figure S1. As a result, no clearly optimal slicer settings for 'Extruder I' were identified.

We iteratively refined the 'Extruder I' prototype to meet the specified QC post-printing. Each development cycle involved empirical evaluation of bioprinting quality, as defined above, through the fabrication of 2D structures (lines and two-layer grids) followed by 3D cylinders with infill (figure 1). Figure 2 presents a comprehensive comparison of extruder advancements, achieved print quality, and the corresponding advantages and disadvantages of each configuration. A table outlining which QC criteria were met by each extruder version can be found in table S4. In the second iteration ('Extruder II', figure 2(B)), we addressed the bending issue (i.e. QC4). Initially, we aimed to reduce the extrusion force by extruding the hydrogel in a molten state at temperatures above 28 °C, where gelatin melts. To achieve this, we designed an aluminum syringe holder compatible with the original FDM printer's heating probe and thermistor (figure 2(B)), allowing for temperature control through the slicer. The bioink composition was first 14% pure gelatin. However, we found that pure molten gelatin lacked sufficient viscosity and was prone to flow before solidifying on the print bed (i.e. failing QC1 and QC2). To address this, we incorporated 5 wt. % alginate into the 14 wt.% gelatin-based hydrogel (a concentration inspired by [19]), which increased viscosity and stabilized the printed structures during cooling (i.e. during gelatin gelation). The hydrogel solidified passively due to ambient air cooling and could then be easily crosslinked

Table 1. Key Ultimaker Cura slicer settings used in this study.

Setting	Tested setting ranges[a]	Settings I[b]	Settings II[c]	Settings III[d]
Initial layer height (mm)	0.05–0.5	0.2	0.2	0.1
Layer height (mm)	0.1–0.28	0.2	0.2	0.1
Initial layer line width (%)	10–200	35	110	35
Line width (mm)	0.1–0.3	0.21	0.21	0.1
Flow (%)	0–1000	900	285	750
Print speed (mm s^{-1})	0–30	2.5	2.5	10
Travel speed (mm s^{-1})	2.5–50	5	30	30
Infill overlap (mm)	−1—+ 1	−0.3	−0.3	−0.25
Retraction distance (mm)	0–30 mm	10	n/a	n/a
Retraction speed (mm s^{-1})	0–50	30	n/a	n/a
Retraction minimum travel (mm)	0–20	1	n/a	n/a
Coasting volume (mm^3)	0–10	n/a	0.21	0.3
Coasting speed (%)	0–100	n/a	50	100
Minimum volume before coasting (mm^3)	0–1	n/a	0.5	0.5
Nozzle temperature (°C)	n/a	20–40	33	28–40[e]

[a] :Slicer setting ranges tested with 'Extruder I' ; hydrogel formulation: 0%–20% wt. gelatin and 0–10 wt. % alginate, varying each component in 1% increments.

[b] : Settings used for 'Extruder II' iteration displayed in figure 2(B); hydrogel formulation: 12% wt. gelatin and 5 wt. % alginate, temperature range: 20 °C–40 °C in 1 °C incrementation.

[c] : Settings used for 'Extruder III' iteration displayed in figure 2(C); hydrogel formulation: 14% wt. gelatin and 2 wt. % alginate.

[d] : Final, optimized settings used for 'Extruder IV' iteration displayed in figure 2(D) and all (cell-laden) bioprinting experiments; hydrogel formulation: 14% wt. gelatin and 0.5–2 wt. % alginate.

[e] : As tested in the PQI evaluation (figure 5). The nozzle temperature was changed if necessary, in particular, to compensate for changes in the environmental temperature (i.e. warm/cold weather). n/a: not applicable.

by submersion in $CaCl_2$ [38]. We observed that the extruder motor struggled to extrude the more viscous hydrogel, so the gelatin concentration was slightly reduced, resulting in a hydrogel blend containing 12 wt.% gelatin and 5 wt.% alginate. This formulation performed well at a nozzle temperature of 33 °C, leading to prints meeting QC1, 2, and 3. This formulation enabled the stacking of layers to approximately 10 mm in height, as depicted in figure 2(B). Table 1 'Settings I' outlines the final slicer parameters for this extruder iteration. Despite these improvements, some extruder bending persisted, significantly impacting print quality during nozzle movements (on- and offsets), which resulted in failure to meet QC4. As a consequence, the cylinder depicted in figure 2(B) was printed as a continuous helix without infill (often referred to as vase mode or spiralized mode), and crossing lines could not be reliably printed. This issue was likely due to the use of PLA in manufacturing certain components of 'Extruder II,' which made it prone to deformation during operation.

To address the ongoing extruder bending issue, we redesigned the extruder in a third iteration ('Extruder III', figure 2(C)) to increase stiffness and improve the on- and offset behavior of the nozzle. This involved sequentially increasing the dimensions of load-bearing components and replacing some parts made of PLA with aluminum ones (figure 2(C)-⑥). Additionally, the plastic syringe was replaced with a 2 ml glass syringe. To prevent glass breakage when the syringe is pressed against the aluminum housing, we incorporated small pads printed out of thermoplastic urethane (TPU), as protective cushions. Concomitantly, the hydrogel composition was adjusted to reduce its viscosity, with the aim of decreasing the extrusion force and, consequently, minimizing bending. According to the literature, alginate is not temperature-sensitive, in contrast to gelatin [39]. We hypothesized that alginate was primarily responsible for the viscosity of our hydrogel in its molten state. As a result, we reduced the alginate concentration from 5 wt.% to 2 wt.% and conducted printing tests at 33 °C. While these modifications improved the nozzle on- and offset behavior (i.e. meeting QC4), the tests revealed that printed lines would flow on the print bed (i.e. failing QC1 and 2), and layers could not be stacked as the walls collapsed before gelation (i.e. failing QC3). To restore printability, the gelatin concentration was gradually increased from 12 to 14 wt.%. At this concentration, gelation occurred rapidly enough at a nozzle temperature of 33 °C, allowing printed lines to maintain their shape and preventing stacked layer collapse (i.e. meeting QC1, 2, and 3). Table 1 'Settings II' outlines the final slicer parameters for this extruder iteration. Modifications introduced to 'Extruder III' in combination with 14 wt.% gelatin and 2 wt.% alginate improved the print quality significantly by resolving issues related to nozzle on- and offset, thereby meeting QC4. These improvements also enabled the successful printing of crossing lines, which had previously been challenging at higher layer heights. The cylinder depicted in figure 2(C) was printed with infill but exhibited a rough, irregular surface finish.

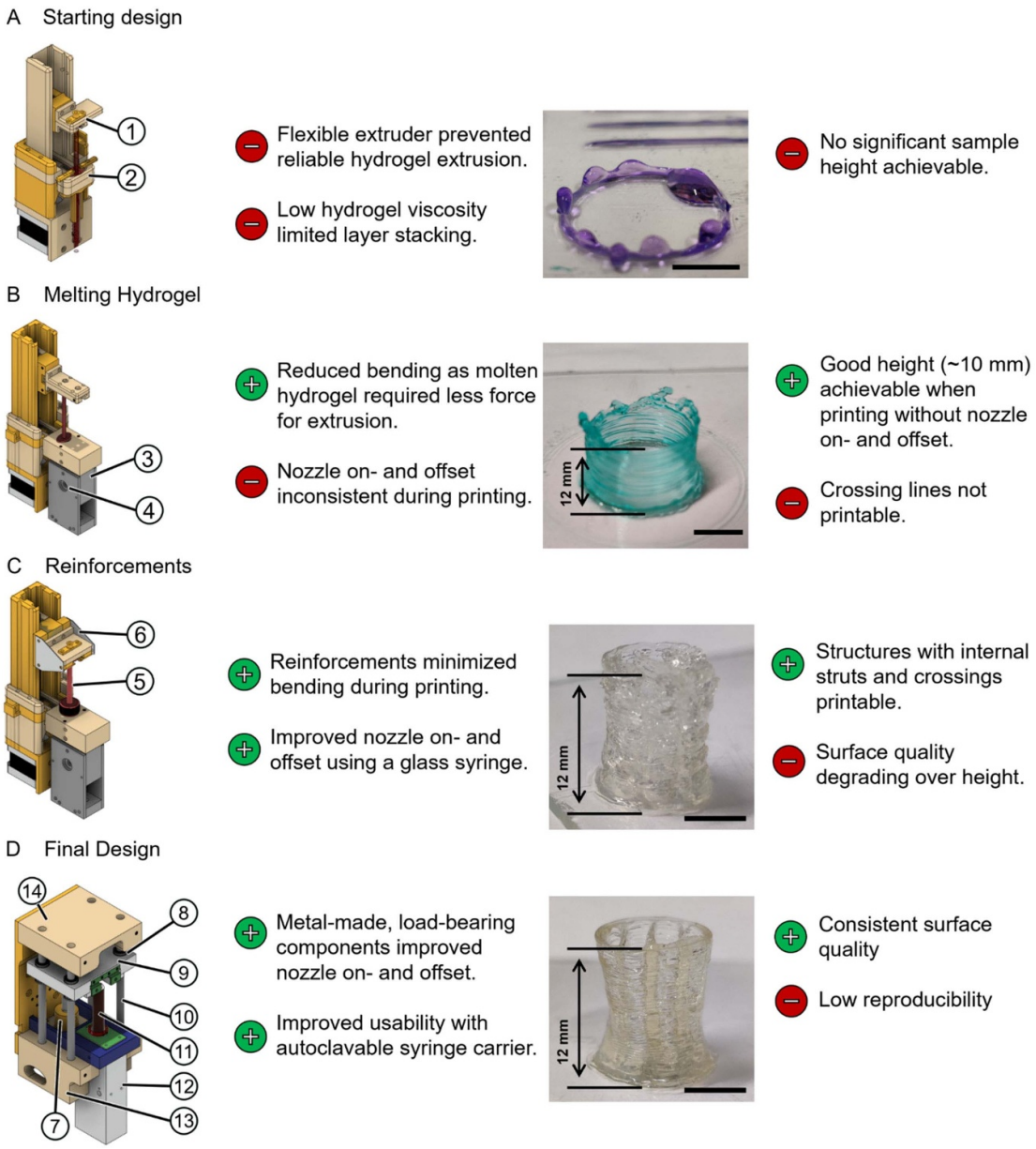

Figure 2. Hardware design iterations of the custom-built extruders (Extruder I–IV) with comments and printed cylinders as examples highlighting the reachable print quality: (A) 'Extruder I', hydrogel: 14% wt. gelatin without alginate. The initial design was mechanically weak, particularly the plunger mechanism (1), and the syringe holder (2) would bend when extruding hydrogel. (B) 'Extruder II', hydrogel: 12% wt. gelatin and 5 wt. % alginate. High extrusion resistance during printing was addressed by replacing the syringe holder with an aluminum block (3), and integrating the thermistor and heating cartridge (4). This allowed thermosensitive hydrogel to be extruded in a molten state by adjusting the slicer settings, reducing the force required for extrusion. (C) 'Extruder III', hydrogel:14% wt. gelatin and 2 wt. % alginate. The plastic syringe was replaced with a 2 ml glass syringe (5), and the plunger mechanism was reinforced with aluminum sheets (6). (D) 'Extruder IV', hydrogel: 14% wt. gelatin and 2 wt. % alginate. This final iteration introduced a complete redesign for rigidity. The drive train was replaced with a custom threaded rod and spindle (7). The plunger mechanism was upgraded to an aluminum block with linear bearings (8, 9) running on stainless steel rods (10). A larger 5 ml glass syringe (11) and a modified heating cartridge (12) were incorporated. The extruder housing (13, 14) was redesigned to accommodate these changes. The hydrogel was extruded in the gelled state at room temperature in (A) and in the molten state at $T > 28\ ^{\circ}C$ in (B)–(D). The slicer parameters are outlined in table 1. In (A) and (B), the hydrogel was supplemented with food dye for better contrast. The extruders' materials in the figure are color-coded: Yellow/Beige: PLA, Red: Syringe, Grey: Aluminum, Green: TPU, Blue: High-temperature PLA. The slicer settings were improved iteratively, with the final settings in table 1. Scale bars: *A, B* = 10 mm, *C, D* = 5 mm. Details on extruder assembly are provided in figure S2–S11 and table S1–S3.

This surface roughness was problematic as it often led to print failures in subsequent layers. We attributed this to the flow effects, hypothesizing that continuous contact between the extruded material and the forming structure is crucial to prevent the formation of surface imperfections, referred to as 'crowning effect'. This crowning effect was highly reproducible and self-propagating, being responsible for most of

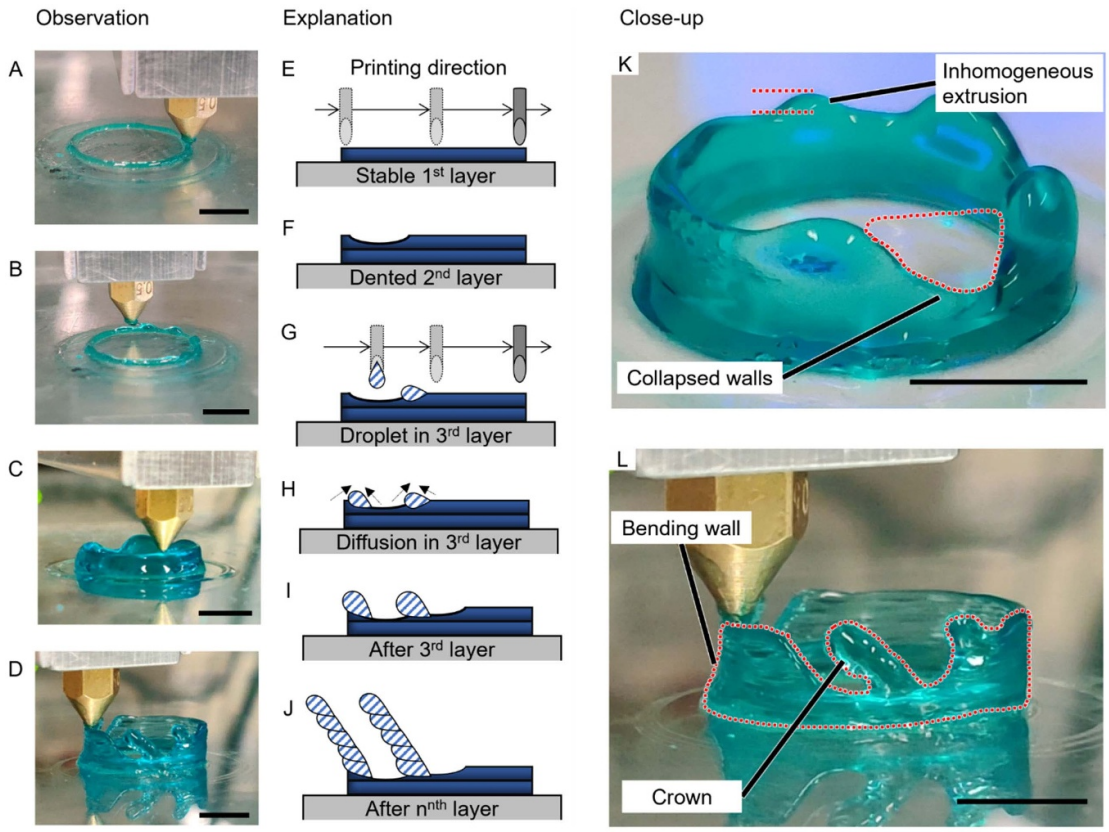

Figure 3. Printing artifact, internally referenced as the crowning effect, caused by mismatched extrusion volume and material flow occurring post-extrusion. (A)–(D) Photographic representation of the sequence of events causing the crowning effect. (E)–(J) Schematic representation of the events displayed adjacently. (A), (E) The first layer was printed successfully. (F) A dent would form on a subsequent layer due to a print error (potentially caused by improper extrusion, mismatched nozzle-print distance, on- and offset delays, bubbles in the hydrogel, etc). (C), (G) In subsequent layers, the extruded material fails to contact the dented area and accumulates at the end of the dent. (H) Diffusion caused by surface interface energy pulls adjacent hydrogel toward the placed drop, causing additional dents to form around it. (E), (I) The lost height around the growing drops results in the cycle restarting. (J) The failure sequence was highly reproducible and has been referenced internally as the crowning effect, as a hollow cylinder would not manifest with closed walls but instead as a crown-like structure. (K) A close-up image of the sample is depicted in (C) from a different angle. Inhomogeneous extrusion and collapsed walls are highlighted (dotted lines). (L) A close-up image of the sample is depicted in (D). The formed crown and a bending wall are highlighted (dotted lines). The scale bars are 10 mm. 'Extruder III', hydrogel: 14% wt. gelatin and 2 wt. % alginate. The printed cylinders are 25 mm in diameter. A 27 G needle was used as the nozzle at a 0.2 mm layer height (in the figure, the needle is not visible as it is inside the heated brass nozzle to protect against cold ambient air).

our print failures. As depicted in figure 3, we propose a sequence of events that contribute to the formation of crown-like structures. To prevent this issue, we determined that maintaining a consistent nozzle-to-layer distance throughout the print was crucial. This required substantial reinforcements to the extruder.

For the final extruder iteration ('Extruder IV'), additional metal components were integrated for improving rigidity as shown in figure 2(D)-⑦–⑩. The drive train was replaced with a custom threaded rod and spindle (figure 2(D)-⑦). The plunger mechanism was upgraded to an aluminum block with linear bearings (figure 2(D)-⑧–⑨) running on stainless steel rods (figure 2(D)-⑩). A larger 5 ml glass syringe was also implemented to increase the print volume. For testing, the hydrogel remained unchanged with 14 wt.% gelatin and 2 wt.% alginate, with slicer 'Settings II' used for slicer configuration. The incorporated modifications enabled the printing of more complex and larger geometries with internal struts, which required frequent nozzle movements, as exemplified in the photo. The resulting cylinder showed an increased height and qualitatively has an improved surface quality (compare photos in figures 2(C) and (D)), successfully meeting our four defined quality criteria. However, printing reproducibility remained poor, as at least one QC criterion was not met in 4 out of 5 prints, with crowning effects observed in most cases (figure 3). This issue was primarily attributed to a suboptimal distance between the nozzle and the forming structure. To address this, the slicer settings were empirically fine-tuned. Key parameters, including flow rate, initial layer line width, and layer height (which are responsible for material extrusion), were adjusted to ensure the nozzle remained consistently close to the forming structure, regardless of the printed height. The print speed was increased from 2.5 to 10 mm s^{-1} (the maximum speed at which

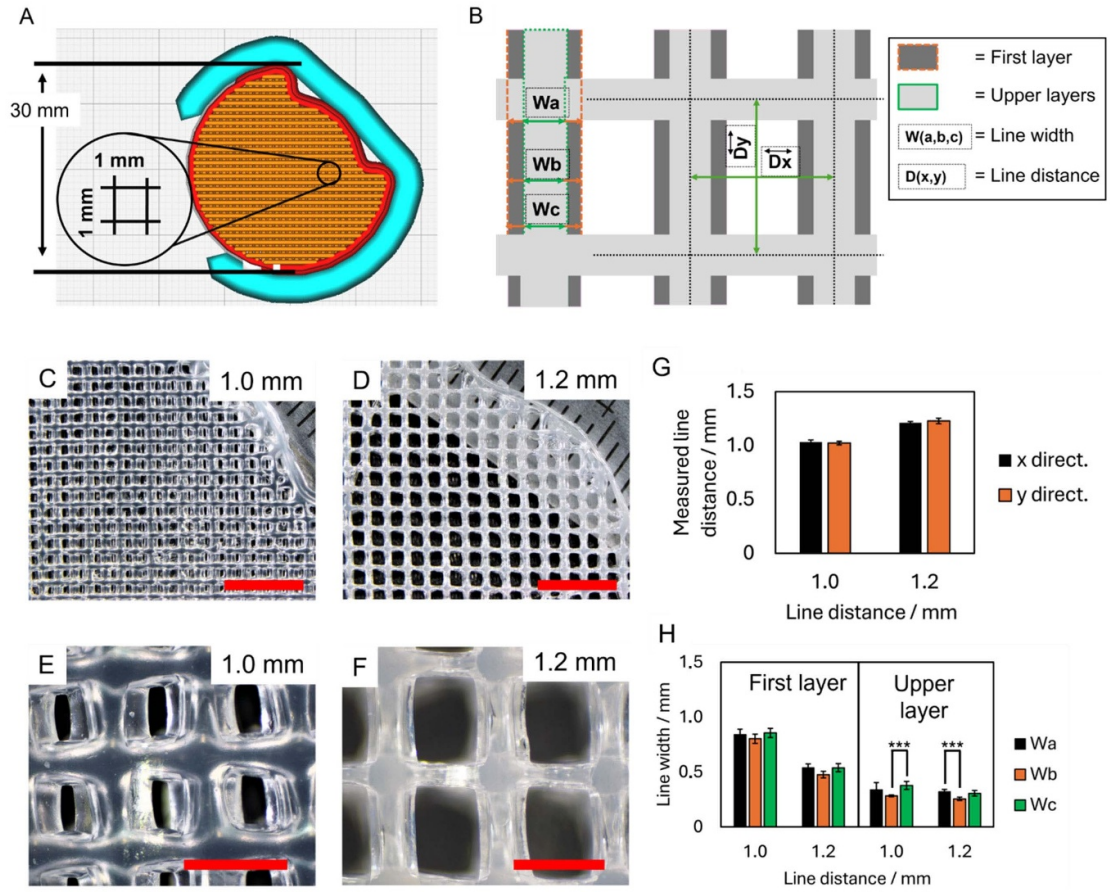

Figure 4. Bioprinter performance evaluation using a test structure. (A) Top-down view of the sliced geometry (1.0 mm line distance is displayed, cylinder is 3 mm tall). (B) Schematic representation of the measurement points in the microscope images, analyzed using the image analysis software FIJI. Movement accuracy was assessed by measuring the distance between the centerlines of the printed lines in the *x* and *y* directions (*Dx, Dy*). Line width consistency was evaluated by measuring the line width at two intersection points where the previous layer was crossed (Wa, Wc) and at a midpoint between these intersections (Wb). (C), (D) Microscopy images (6.7x magnification) of printed constructs with two different wall line distances. (E), (F) Close-up views of the walls in the respective samples. (G) Measured line distances at five measurement points in the x and y directions. (H) Line widths at different positions along the walls (Wa, Wb, Wc) for the first layer ($n > 4$) and the upper layer ($n > 8$). Scale bars: 5 mm in (C), (D) and 1 mm in (E), (F). Statistical significance was defined as $^{***}p \leqslant 0.001$.

the material could still be extruded) to reduce print time and minimize drying, which we assumed would shrink the sample and hence contribute to an inconsistent nozzle-print distance. Additionally, the coasting speed was raised from 50% to 100% of the print speed to maintain consistency, as speed fluctuations during printing were believed to increase the likelihood of crown formation. These adjustments led to improvements in reproducibility (i.e. only 1 out of five prints displayed crowning effects). The final slicer settings are presented in table 1, 'Settings III.' Unless stated otherwise, 'Settings III' were used for all subsequent printing experiments with 'Extruder IV.'

The 'Extruder IV' prototype, combined with the optimized slicer settings, enabled the fabrication of more complex, multi-layered structures while meeting all four defined quality control criteria—a significant advancement over previous extruder prototypes and slicer configurations. To further assess the system's capabilities, we evaluated its achievable resolution by testing its ability to execute precise *x*–*y* movements and maintain a stable extrusion rate across multiple layers, ensuring accuracy in all three dimensions (figure 4). Specifically, we printed two 3 mm-tall cylinders with a grid infill pattern, varying the line distances (1 mm and 1.2 mm), to assess consistency in line width and overall structural integrity (figure 4(A)). Microscope images of the printed constructs (6.7× magnification) are shown in figures 4(C)–(F). The printed structures were then quantitatively analyzed using the image analysis software FIJI (figure 4(B)). The results in figure 4(G) indicate that the measured line distances in both *x* and *y* directions closely matched the intended values of 1.0 mm (actual: 1.03 ± 0.005 mm) and 1.2 mm (actual: 1.22 ± 0.038 mm). This was expected as the original printer's *x* and *y* movement systems were unaltered. For the sample printed at 1.0 mm wall spacing, the first-layer line width was measured at 0.83 ± 0.022 mm and the upper-layer width

at 0.33 ± 0.039 mm (figure 4(H)). The increased width of the first layer was likely due to the initial hydrogel spreading perpendicularly on the build plate before solidification. In contrast, in the upper layers, the material likely flowed downward, making it less detectable in the measurement. This is further supported by variations in upper layer line widths along the wall length, with statistically significant deviations indicating that the area bridging between holes (i.e. Wb) was thinner than the other measured points (Wa, Wc: ∼0.36 ± 0.05 mm, Wb: ∼0.28 ± 0.009 mm). Since material extrusion was presumably consistent during printing, it is likely that some hydrogel flowed downward into previous layers, as previously described by He *et al* [33]. A similar trend was observed in the sample printed with 1.2 mm wall spacing, where the first-layer width was 0.52 ± 0.030 mm and the upper-layer width was 0.29 ± 0.028 mm (uniformity across line width: Wa, Wc: ∼0.31 ± 0.022 mm, Wb: ∼0.26 ± 0.015 mm). The difference between the first and upper layers was smaller in this sample, suggesting that the reduced spacing in the 1.0 mm sample may have influenced the initial hydrogel spreading. One possible explanation is that surface tension played a more significant role in the first layer when the wall lines were positioned closer together.

These findings validate the bioprinter's high movement accuracy and its capability to produce thin walls (i.e. ∼ 0.3 mm, figure 4(H)), which are well-suited for efficient oxygen and nutrients diffusion required while cultivating cells in the printed structures. The increased width of the first layer was considered negligible due to the minimal height of the affected area. In their systematic review, Tarassoli *et al* compared the printing resolution and speed of commercially available and custom extrusion-based bioprinters [36]. Among the listed printers, eight were faster, six were slower, and nine had a comparable print speed to our system (i.e. 10 mm s^{-1}). Similarly, nine exhibited a lower printing resolution, four achieved a higher resolution, and 23 had a comparable resolution (i.e. 0.3 mm). These values are consistent with the observations published by Guida *et al,* who, among others, recently reviewed the printing resolution of 28 extrusion-based bioprinters [26]. However, the achievable height of bioprinted samples is rarely mentioned in the literature, making direct comparisons challenging.

To conclude, achieving consistent surface quality across multiple stacked layers is a delicate process heavily reliant on maintaining a constant nozzle-to-layer distance through highly optimized slicer settings. The successful printing of structures exceeding 10 mm in height with consistent surface quality demonstrated the suitability of the repurposed FDM-printer with a modified extruder for high-quality hydrogel printing. The development of this printer was time-consuming, as most optimizations were based on trial-and-error testing. This highlights the need for establishing a quality benchmark to accelerate the optimization process.

2.2. Development of a quality benchmark for bioprinting optimization

He *et al* and Ouyang *et al* correlated print temperature (i.e. nozzle temperature) with flow effects during printing, which could be responsible for the above-mentioned low reproducibility we observed. As we only roughly estimated the print temperature until this point, we attempted to improve the printing reproducibility by using the printability method proposed by Ouyang *et al* [32] to determine the optimal nozzle temperature for the previously tested hydrogel composition (i.e. 14 wt.% gelatin-2.0 wt.% alginate). We assessed print accuracy by creating two-layer grid structures (i.e. simple geometric structure, figure 1) at nozzle temperatures of 29 °C (i.e. the lowest temperature where the chosen bioink remained liquid), 38 °C (i.e. the highest temperature safely compatible with cells), and 34 °C (an intermediate temperature). The results are depicted in table 2 and figure 5(A).

Based on the morphology of the interconnected channels in the printed grid structure, three distinct flow regimes were identified on the print bed: square, dumbbell, and rectangular (figure 5(A)). A perfect print, accurately replicating the intended geometry (figure 1(A)), resulted in a square with regular edges, termed 'square regime'. This ideal state was achieved solely when material flow on the print bed ceased quickly due to solidification, a condition realized at a nozzle temperature of 29 °C. Increasing the printing temperature to 34 °C extended the cooling time of the top layer, rendering it susceptible to flow effects and causing it to sink between the underlying layer's lines. When viewed from above, these printed grids exhibited a dumbbell shape, as first described by *He et al* [33]. At 38 °C, the top layer entirely collapsed onto the print bed, elongating the grid's holes into a rectangular form. Hydrogel printability was semi-quantified as proposed by Ouyang *et al* [32] by measuring the perimeter and surface area of the interconnected channels to calculate a 'printability score'. For this purpose, top-down photographs of the printed grids were captured and subsequently subjected to automatic analysis using the image analysis software FIJI. The printability scores calculated according to Ouyang *et al* [32] were fairly similar across the outer temperatures of 29 and 38 °C (table 2), despite the observable structural differences (figure 5(A)). This indicated that the proposed calculation was not fully adequate for our purpose. To address this, we refined the printability evaluation by including two additional parameters in the calculation and assigning terms to specific flow regimes. Square Ratio (SR, equation (1), figure 5(B)) quantified how square a

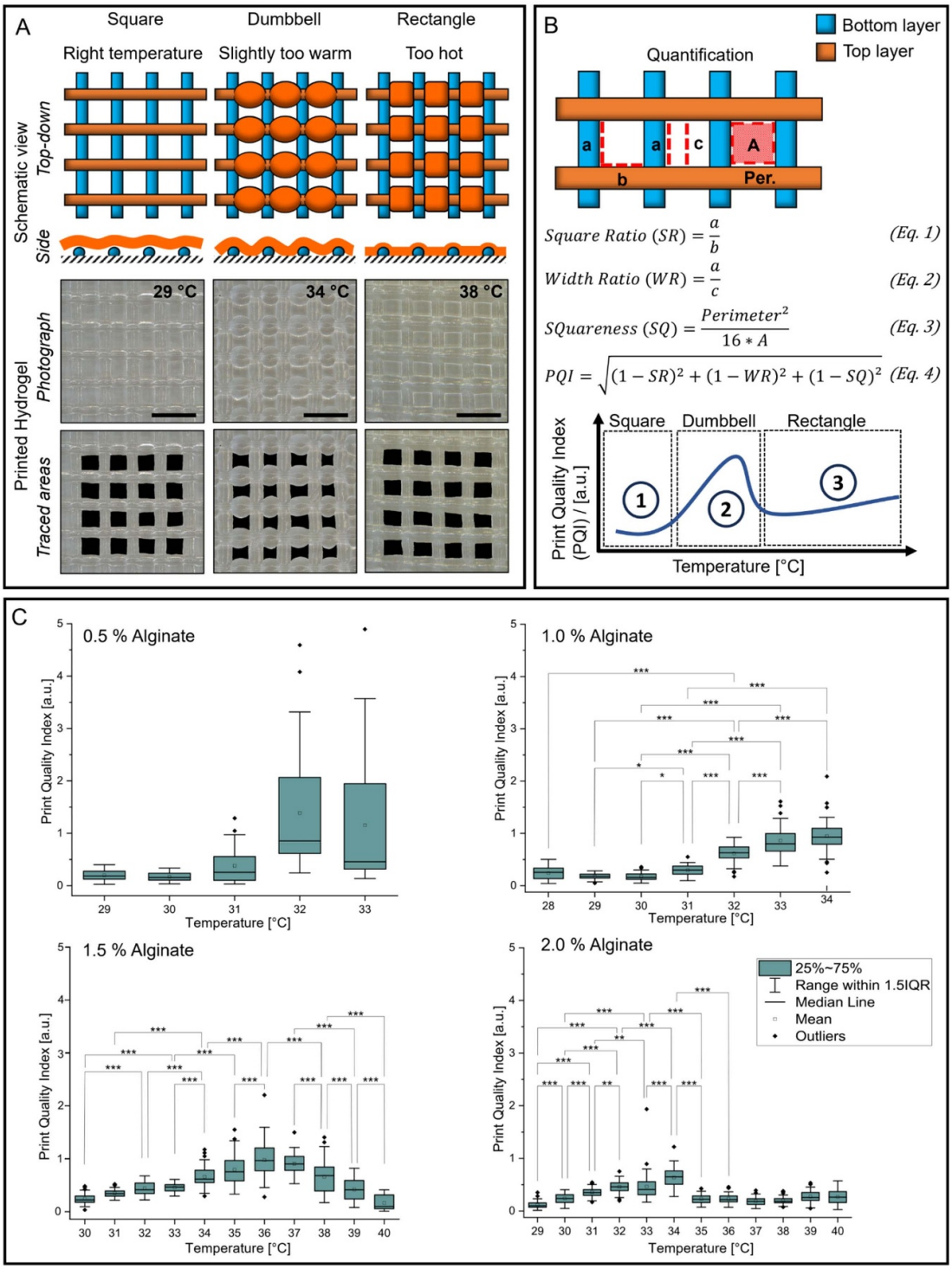

Figure 5. Print quality index (PQI) for fine-tuning nozzle temperature of a given hydrogel. (A) Two-layer grids (20 mm × 17 mm, grid line distance: 1 mm) printed with 14% gelatin and 2% alginate at a nozzle temperature of 29 °C (left), 34 °C (center) and 38 °C (right). The slicer settings: 'Settings III' (table 1). The samples were crosslinked with $CaCl_2$ before top-down images were taken. Scale bars are 5 mm. (B) Quantification of flow regimes (SR: square, WR: dumbbell, SQ: rectangle) and PQI. The scheme displays the theoretical PQI-curve of any tested hydrogel. (1) Displays the square regime where good printing can be achieved. (2) Displays the dumbbell regime, where too high nozzle temperatures prevent good printing quality. (3) Displays the rectangular regime, where the top layer has completely sunk to the build plate. (C) PQI of 14% gelatin and X %-alginate samples at different printable temperatures. Three independent 2-layer grid structures were printed for each temperature, and sixteen interconnected channels were evaluated per grid. Whiskers show the interquartile range. □: mean; -: Median; ♦: PQI for a specific grid.

hole was by comparing channel side lengths. Width Ratio (WR, equation (2), figure 5(B)) assessed the dumbbell regime by comparing the narrow channel width at the dumbbell peak to its sides. The SQuareness (SQ, equation (3), figure 5(B)) compared the ratio of a channel's perimeter and area to that of an ideal square, i.e. measured the channel rectangularity. SQ considered unexpected printing artifacts, like

Table 2. Comparison between Ouyang *et al*'s Printability score [32] and our print quality index (PQI) to evaluate print quality.

Temperature	Printability score[a]	Print quality index (PQI)
29 °C	1.05 ± 0.04	0.12 ± 0.02
34 °C	1.44 ± 0.11	0.64 ± 0.04
38 °C	1.06 ± 0.04	0.2 ± 0.01

A hydrogel composed of 14% gelatin and 2% alginate was used for these experiments. A comparative evaluation of the efficiency of both methods is provided in the SI (figure S12).

[a] : Printability score: a value of 1.0 represents the best achievable printability. Print quality index (PQI): the lower the value, the better the print accuracy.

jagged or rounded corners, common when printing alginate/gelatin-based hydrogels at low temperatures [19, 32]. Perfectly formed channels exhibited a square shape, i.e. a value of 1 for SR, WR, and SQ, respectively. The Print Quality Index (PQI, equation (4), figure 5(B)) is designed to combine the information contained in the individual terms (i.e. SR, WR, and SQ) in a manner that is highly sensitive to deviations from the intended geometry. It provides a rapid assessment of printing temperature suitability. We anticipate a bell-shaped relationship between PQI and temperature as the morphological error is highest in the dumbbell regime. Low PQI values correspond to superior gelation conditions, resulting in higher-quality prints. A comparative analysis of the two evaluation methods revealed that the PQI offers a more comprehensive assessment than the printability method proposed by Ouyang *et al.* The latter frequently overestimates printability values, making it less reliable for accurate temperature determination (figure S12).

When printing cell-laden hydrogels, careful selection of the bioink formulation is essential, as it depends on the specific cell type used, which in turn requires fine-tuning of the print temperature to get the highest print fidelity achievable on a specific machine [40]. We hypothesized that the PQI method could help determine the optimal printing temperature while ensuring consistent high-quality prints. To test this hypothesis, we focused on optimizing the printing performance of a wide range of alginate/gelatin-based hydrogels, used as model bioinks in our system. Our initial evaluation concentrated solely on printability, as a hydrogel's ability to support cell proliferation is influenced not only by its composition but also by the specific cell type being cultivated [41–43]. To evaluate the broader applicability of the PQI method, we expanded our selection to include formulations beyond those specifically suited for the model cells used in this study. The impact of the hydrogel composition on cellular proliferation is explored in a later chapter.

To this end, the alginate concentration was varied between 0.5 wt.% and 2.0 wt.%. Hydrogel formulations exceeding 2.0 wt.% alginate were not investigated due to extrusion difficulties encountered at the 2.5 wt.% level, resulting from increased viscosity, as observed during the extruder development (figure 2). Gelatin concentration was held constant at 14% as this level proved sufficient for gelation at room temperature and maintenance of the stability of printed constructs prior to alginate crosslinking with $CaCl_2$. To assess the reproducibility of the printing process, three replicates were printed for each temperature/alginate-concentration combination using freshly prepared hydrogels. The lowest possible print temperature was defined as the point at which the hydrogel began to gelate while still within the nozzle, preventing extrusion. The highest possible print temperature was determined as the temperature at which the hydrogel maintained fluid on the print bed and deviated from the desired shape after deposition. Sterilized hydrogels were used to ensure consistency with the upcoming bioprinting experiments and culturing of cell-laden samples [25, 44]. To achieve sterility, alginate and gelatin powders were UV-irradiated before being dissolved in sterile DPBS under aseptic conditions. We then proceeded to generate two-layer grid structures and systematically evaluated the geometric accuracy across the entire printable temperature range (28 °C to 40 °C), as shown in figure 5(C).

Hydrogels formulated with 0.5 and 1.0 wt.% alginate printed at temperatures $\leqslant$ 31 °C have PQI values below 0.5, reflecting a square regime. At temperatures between 32 and 34 °C, the PQI values increased to up to 2, indicating a dumbbell regime. Temperatures exceeding 34 °C caused these formulations to collapse into puddles, preventing PQI assessment. In contrast, hydrogels containing 1.5 and 2.0 wt.% alginate produced two-layer grid structures, accurately replicating the intended geometry at extrusion temperatures up to 39 and 40 °C, respectively. The derived PQI values showed a bell-shaped development, hence following the theoretical relationship of PQI and temperature shown in figure 5(B). As the printed structures were not actively cooled, variations in PQI values among replicates (figure 5(C)) could be attributed to inconsistencies in the solidification process influenced by ambient temperature fluctuations. Potential inconsistencies in hydrogel preparation may also have contributed to printing variability. On the print bed, the stability of the printed structure is related to the hydrogel viscosity, determined in our case by the alginate concentration and the surrounding temperature, which initiates gelatin gelation. This is supported by the observed trend in printed samples containing 0.5–2.0 wt.% alginate, where the variability in PQI values between replicates decreased

with increasing alginate concentration, corresponding to the hydrogel viscosity. Our systematic analysis demonstrated that a hydrogel composed of 14 wt.% gelatin and 2 wt.% alginate yielded improved print quality consistency and enhanced tolerance to ambient temperature variations.

2.3. Achieving high-quality 3D structures using the PQI method

The ideal printing temperature for a given hydrogel must balance two opposing factors. First, the time required for a freshly printed line to reach the sol-gel transition point (the temperature at which the material can no longer flow) should be minimized to reduce the risk of flow-induced print failures, which favors a lower printing temperature. Conversely, higher temperatures are assumed to reduce bioink viscosity, thereby decreasing the shear forces on the cells and improving their viability, as higher temperatures are thought to be more cell-friendly [32]. As a compromise, the upper-temperature limit is set by the onset of the dumbbell regime, where the print quality deteriorates, as determined using the results of the PQI method presented above (figure 5). Thus, for a given hydrogel formulation, the ideal printing temperature should be 1 °C lower than the onset of their respective dumbbell regime (1 °C being the smallest, adjustable temperature increment of the system). Given that the suitable print temperature determined by the PQI method is derived from data obtained during 2D printing, we investigated whether these insights could be extrapolated to the 3D printing of more complex structures, such as cylindrical test grids. After printing, the samples were first qualitatively assessed against the defined print quality criteria (QC1 to QC4) before being measured using the image analysis software FIJI, with their actual dimensions compared to the intended values. We first assessed the suitability of the PQI method for selecting the optimal print temperature for a given hydrogel formulation. To this end, cylindrical structures with grids (intended diameter: 15 mm, intended height: 3 mm, print time: ∼10 min) were fabricated using hydrogels composed of 14 wt.% gelatin with 0.5–2.0 wt.% alginate (figures 6(A) and (B)). As indicated by the PQI results presented in figure 5, the optimal printing temperatures were identified as follows: 30 °C for 0.5 wt.% alginate, 31 °C for 1.0 wt.%, and 33 °C for 1.5 and 2.0 wt.% alginate. Printing in the rectangular PQI regime (e.g. at 40 °C for 1.5 wt.% alginate) is not recommended, as excessive heat may lead to cellular damage and an increased risk of flow-induced print failures due to delayed gelation. All printed structures met our print quality acceptance criteria. The measured line widths ranged between 0.5 and 0.6 mm, while the height varied from 3.0 to 3.3 mm and the diameter from 15.3 to 16.1 mm, depending on hydrogel composition. The deviation from the intended height and diameter values was always less than 10% in both cases. Across all formulations, the average measured height was 3.18 ± 0.07 mm, reflecting a 6.05% deviation from the intended geometry, while the average measured diameter was 15.65 ± 0.21 mm, corresponding to a 4.3% deviation (table S5). Despite these minor deviations, the geometric and dimensional accuracy of the printed structures was considered satisfactory. These results confirm that the PQI method provides a reliable framework for selecting the optimal print temperature for a given bioink formulation.

To determine whether PQI-selected print temperatures remain applicable to larger structures, and to evaluate the reproducibility of the developed system, we printed three test constructs (intended diameter: 15 mm, intended height: 7.5 mm, print time: ∼20 min) using 14 wt.% gelatin—0.5 wt.% alginate at 30 °C (figure 6(C)). As summarized in table S6, all structures met the print quality acceptance criteria. Notably, sample drying did not negatively impact the printing performance. For each sample, the achieved height deviated from the intended value by less than 5%, while the diameter deviated by less than 1.1%. Across all samples, the average measured line width was 0.40 ± 0.04 mm, while the average height was 7.61 ± 0.21 mm, corresponding to a 1.45% deviation from the intended value. The average diameter was 14.96 ± 0.24 mm, with a 0.24% deviation from the intended value. These findings establish that PQI-based temperature selection remains valid for taller 3D-printed constructs and that the repurposed FDM printer is capable of fabricating larger-scale biofabricated structures with high geometric accuracy.

Collectively, these results demonstrate the efficacy of the PQI method in optimizing print temperature for high-quality 3D bioprinted structures, ensuring both geometric precision and dimensional accuracy. Furthermore, the ability to extend PQI-derived temperature selection from 2D to 3D printing highlights its robustness as a tool for optimizing bioink formulations in bioprinting applications. The PQI method provides a rapid, efficient approach for determining the optimal printing temperature of any alginate/gelatin-based thermosensitive bioink by monitoring gelation behavior, particularly useful in the absence of rheological instrumentation. Our results confirm that diverse alginate/gelatin hydrogels can be printed successfully without compromising quality, provided slicer settings are properly adjusted. The PQI's evaluation broad applicability is especially useful in developing new bioprinting protocols. For instance, since hydrogel sterilization methods can alter print characteristics [25], the PQI method can help adjust slicer settings to accommodate flow behavior changes, provided that the hydrogel's phase-change property remains intact. Similarly, the PQI could aid in optimizing slicer settings when (i) using

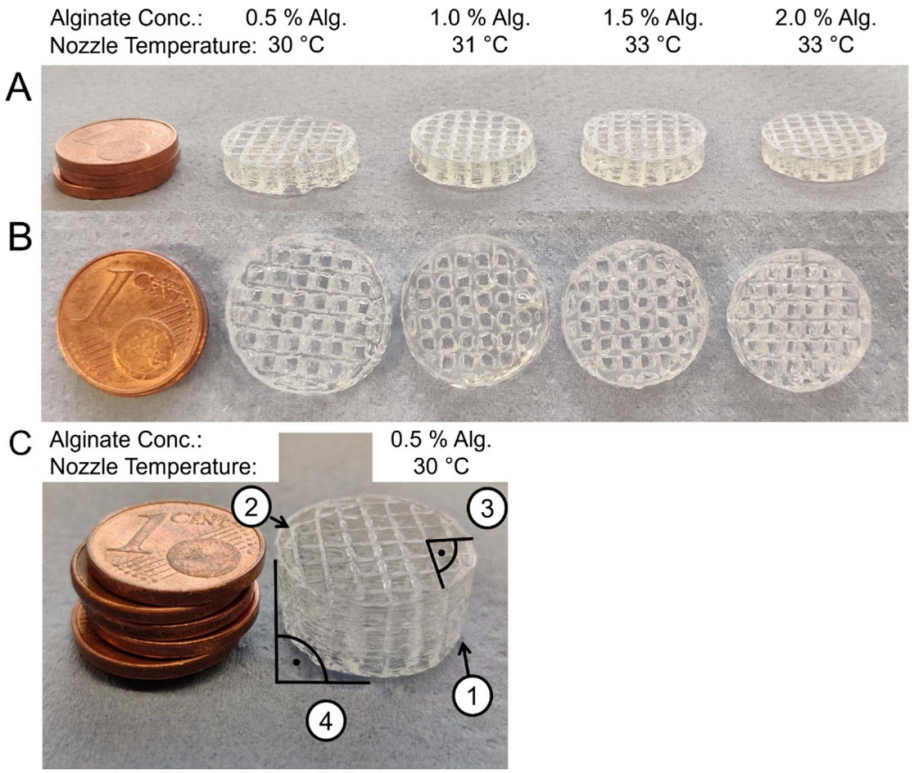

Figure 6. Example prints of different hydrogel compositions (14% gelatin/X %- alginate samples) printed at their optimal nozzle temperatures, as determined with the PQI method. Each concentration and temperature condition was tested with three prints, all exhibiting consistent quality. (A) Side view. (B) Top view. The coins (diameter: 16.25 mm) provide a size reference. The printed cylinders are 3 mm tall and 15 mm in diameter (achieved height: 3.18 ± 0.07 mm, achieved diameter: 15.65 ± 0.21 mm, table S5), with an estimated print time of ∼10 min per cylinder, as calculated by the slicer. (C) To demonstrate scalability, a larger, 7.5 mm-tall cylinder (0.5% alginate, 75 layers) was printed (achieved height: 7.61 ± 0.21 mm, achieved diameter: 14.96 ± 0.24 mm (see table S6). The structure maintains high surface quality on the outer wall (1) and the top layer (2), confirming consistent layer stacking without extrusion errors. Sharp 90° corners (3) indicate stable nozzle-to-print distance, while the straight outer walls (4) reflect uniform extrusion behavior. The total print time for this larger structure was approximately 20 min.

alternative bioink formulations, (ii) incorporating additional bioink components (e.g. to enhance cellular growth), ensuring printability is maintained despite modifications to the formulation.

2.4. Tailoring hydrogel composition for optimal support of cell growth and viability

In the next step, we assessed the influence of alginate concentration within the previously employed hydrogel formulations on cellular proliferation. As previously reported, cellular proliferation within alginate hydrogels tends to decrease as alginate concentration increases [45]. Our goal was to identify a hydrogel formulation that is both accurately printable while providing a suitable microenvironment for robust mammalian cell growth. To assess hydrogel formulation suitability, we used recombinant human epithelial liver cancer cells stably expressing the EGFP (HuH7^{EGFP}) as a model system. The use of a cell line ensured high reproducibility and comparability across experimental runs, while eliminating the donor variability associated with primary cells. HuH7 cells typically form aggregates in non-adhesive environments and were used here to evaluate which hydrogel formulation optimally supports cell growth without restriction.

To isolate the impact of the alginate concentration on cell growth within the hydrogel and eliminate confounding variables such as shear stress, which could vary with hydrogel viscosity during bioprinting, we employed a stamped cell-laden hydrogel approach (figure S13). This method ensured consistent starting conditions across different alginate formulations. Alginate concentrations ranged from 0.5 to 2 wt.% in DPBS. The upper alginate limit was imposed by our bioprinter's extrusion capabilities (figure 2). The minimum concentration was determined based on the printability requirements outlined in previous chapters. As detailed in Section 2.1, pure molten gelatin exhibited insufficient viscosity for printing using our modified FDM printer (figure 2(A)). The gelatin concentration was left unchanged at 14 wt.% as its thermal gelation properties were required for bioprinting with our system. Cell-laden stamped hydrogel dimensions (diameter: 7.5 mm, height: 0.5 mm) were chosen to fit micro-well plates and mimic the thickness of upcoming bioprinted grid infill lines.

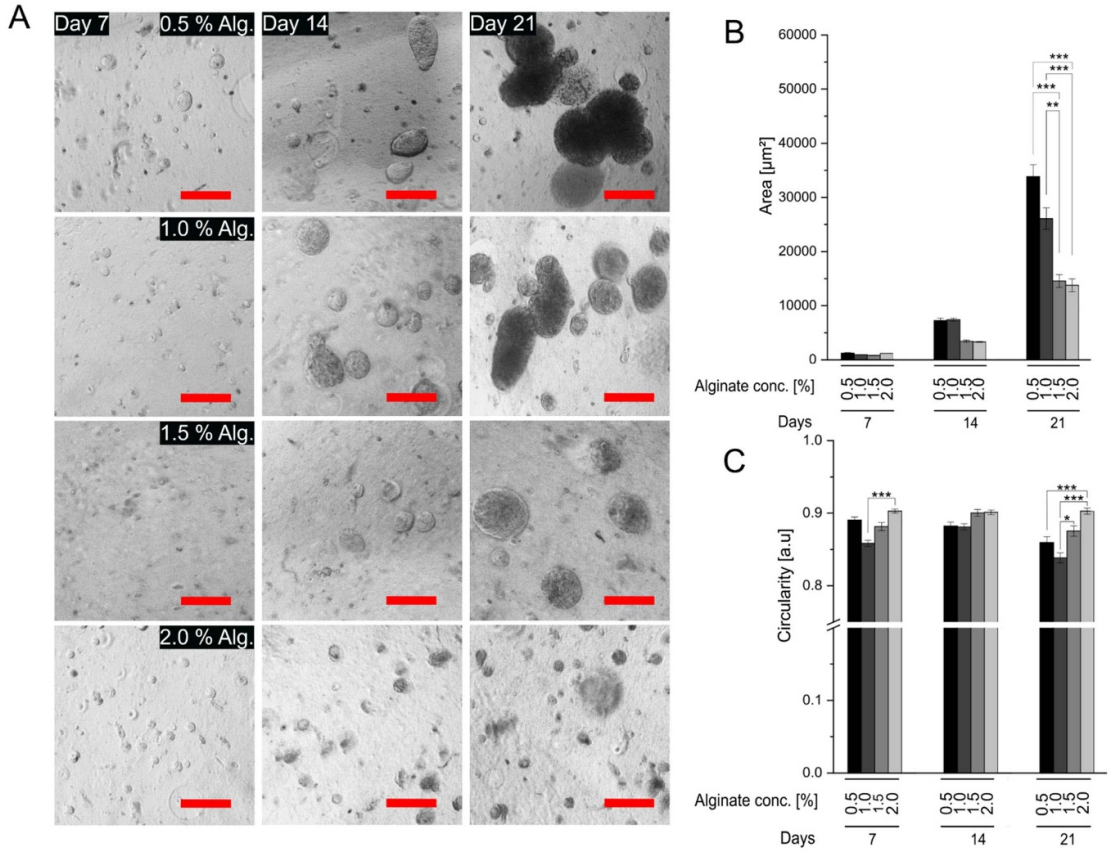

Figure 7. Growth behavior of human hepatoma cells (HuH7^{EGFP}) regarding cellular aggregates shape and size in cell-laden stamped hydrogels. The stamped hydrogels composed of 14 wt.% gelatin and various amounts of alginate were cultivated in 24-well plates. Culture medium was exchanged every 2–3 d. (A) Representative photographs of cellular aggregates after 7, 14 and 21 d of cultivation. Scale bars = 50 µm. Size (B) and circularity (C) of aggregates in the hydrogels at different alginate concentrations. Four or more stamped hydrogels were produced for each alginate concentration. The size and circularity development of more than 10 aggregates were tracked per film over 21 d. Stamped hydrogel size: diameter, 7.5 mm—height, 0.5 mm.

Each stamped hydrogel contained approximately 2000 cells (equivalent to about 4500 cells cm^{-2} or 10^5 cells cm^{-3}). Hydrogels were cultured in 24-well plates for up to three weeks with medium exchange every 2–3 d. Of note, for the bioink preparation, cells were directly resuspended in DPBS without additional washing steps to avoid additional stress for the cells.

Microscopic evaluation was conducted throughout the cultivation to assess cell aggregate size and shape (i.e. circularity). Aggregate size was quantified by surface area due to the irregular, elongated morphology that precluded accurate diameter measurement (commonly used in the peer-reviewed literature). Circularity was used as a metric of aggregate roundness. High circularity (i.e. circularity approximating a value of 1) and small sizes were interpreted as indicative of restricted growth, while lower circularity values and larger sizes suggested greater freedom of expansion. The results are presented in figure 7.

Figure 7(A) shows representative cell aggregates after 21 d of cultivation. Cell proliferation (i.e. aggregate area) was notably higher at alginate concentrations below 1.5 wt.%, with this trend becoming more pronounced over time. A statistically significant difference in growth was achieved after 21 d (figure 7(B)). The resulting aggregate sizes align with those reported in the literature for tumor cell-derived spheroids [46]. While alginate concentration did not significantly impact the aggregate shape, which remained mostly spherical with a circularity between 0.8 and 0.9, cell aggregates formed in lower alginate concentrations exhibited less defined edges after 21 d of cultivation (figure 7(C)). Previous studies have linked cell proliferation and aggregate growth to hydrogel stiffness [41–43]. Our observations support this, as the 0.5 wt.% alginate hydrogel formulation appeared less stiff than the 2.0 wt.% alginate ones during handling. Since we did not measure the hydrogels' mechanical properties, it can only be assumed that higher alginate concentrations lead to higher mechanical gel strength. Considering the HuH7 parental cell line's known preference for softer microenvironments [47, 48], the hypothesized increased stiffness of hydrogel formulated with

Table 3. Cellular viability values obtained from fluorescence microscopy analysis of single-layer constructs.

Storage time/min	Cellular viability/%	
	Control sample[a]	Printed sample[a]
0	93.9 ± 2.3	89.3 ± 2.7
10	91.7 ± 4.	83.7 ± 6.0
20	93.1 ± 1.9	77.5 ± 6.2

[a] : Data represent mean values ± SD, $n = 3$. Differences between control and printed samples were not statistically significant.

higher alginate concentrations may have impeded cellular growth, contributing to the smaller aggregate size observed. Based on these findings, hydrogel formulations containing 14 wt.% gelatin and 0.5–1.0 wt.% alginate were found appropriate for subsequent bioprinting of HuH7^{EGFP} cells.

2.5. Bioprinting case study

Building upon the above-described bioprinter design, optimized slicer settings (PQI method; figure 5), and identified cell-supportive hydrogels (14 wt.% gelatin, 0.5 and 1.0 wt.% alginate; figure 7), we investigated the 3D bioprinting of cell-laden constructs. To evaluate the impact of extrusion on cellular viability, we first bioprinted single-layer lines using HuH7^{EGFP} cells at a concentration of 10^6 cells ml^{-1} onto microscope slides (hydrogel: 14 wt.% gelatin, 0.5 wt.% alginate). Dead cells were counterstained with propidium iodide, and fluorescence microscopy was used to determine the live-to-total cell ratio. As control, bioink was maintained under identical conditions but manually transferred onto microscope slides using a sterile spatula instead of being extruded through the nozzle. Given the approximate 10 min print time per sample (as in figure 6), we assessed different storage durations—i.e. the time cells remained in the bioink before printing or manual transfer—of 0, 10, and 20 min. Each condition was tested in triplicate to ensure reliability. The resulting viability values are summarized in table 3.

The experiment demonstrated that cellular viability remained high after extrusion. However, a statistically non-significant downward trend was observed when the bioink was stored in the syringe for 20 min. In comparison, the control sample consistently maintained viability above 90%, suggesting that the observed decrease was likely due to the shear forces encountered during extrusion, rather than factors such as oxygen or nutrient depletion. Although, we cannot completely rule out the possibility that extended storage in the syringe before printing may increase cellular sensitivity to shear stress. These findings align with previously reported viability ranges of 40%–80% for extrusion-based systems, as reviewed by Xu *et al* in their study on cell damage during bioprinting [49].

We printed cell-laden gridded cylinders using the modified FDM-printer described above operating within a biosafety cabinet. This specific macroporous geometry (diameter: 15 mm, height: 3 mm), shown in figures 8(A) and (B), was selected to fit within the wells of a standard 6-well tissue culture plate, where the samples were cultured. Larger cell-laden constructs were considered not practical due to the limitations of our static cultivation method. Although a 10 mm construct would physically fit within a standard six-well plate (well height: 16.5 mm, according to the manufacturer), it would require more than the recommended maximum of 3 ml of medium to fully cover the structure and prevent hydrogel drying. This excess volume could lead to diffusion limitations, potentially impeding cell proliferation at the base of the construct. Consequently, we limited the bioprinted construct size to 3 mm in height and 15 mm in diameter (with the grid infill line width estimated at ∼400 µm–500 µm based on microscope images, print time: ∼10 min). Scaling beyond these dimensions would likely require specialized perfusion bioreactors to overcome diffusion constraints, as standard static culture methods (e.g. six-well plates) do not provide sufficient nutrient exchange.

Hydrogels containing 14 wt.% gelatin and 0.5 wt.% alginate (print temperature, 30 °C) or 1.0 wt.% alginate (print temperature, 31 °C) were used. The cellular load in the bioink (i.e. hydrogel + cells) was 5×10^4 HuH7^{EGFP} cells ml^{-1} in all cases. Printed cell-laden hydrogels were crosslinked by submerging into 0.1 M $CaCl_2$ for 3 min and then cultured in the 6-well plates under static conditions. The cell culture medium was exchanged every 2–3 d. The designed grid geometry was expected to have low diffusion limitations due to its hole structure, creating a supportive environment for promoting cell proliferation. Cell proliferation was monitored over 25 d by fluorescent microscopy analysis; representative results are depicted in figure 8(C). Importantly, HuH7^{EGFP} cells produce EGFP as a non-covalently bound cytoplasmic protein. Upon cell death, EGFP is released into the culture medium. Consequently, only viable cells with intact plasma membranes can be detected through fluorescence microscopy.

Both hydrogel formulations demonstrated successful 3D high-quality printability (i.e. meet our defined QC1 to QC4 acceptance criteria). The incorporation of cells did not noticeably alter print quality compared to cell-free controls. These results align with previous studies [50] suggesting that the low cell density within the bioink had a minimal effect on the printing process. A significant challenge encountered during cultivation was the presence of air bubbles entrapped between the grid lines (figure 8(D)), presumably hindering local cell proliferation. Despite attempts to remove these bubbles, they persisted for approximately 10 d before dissipating naturally.

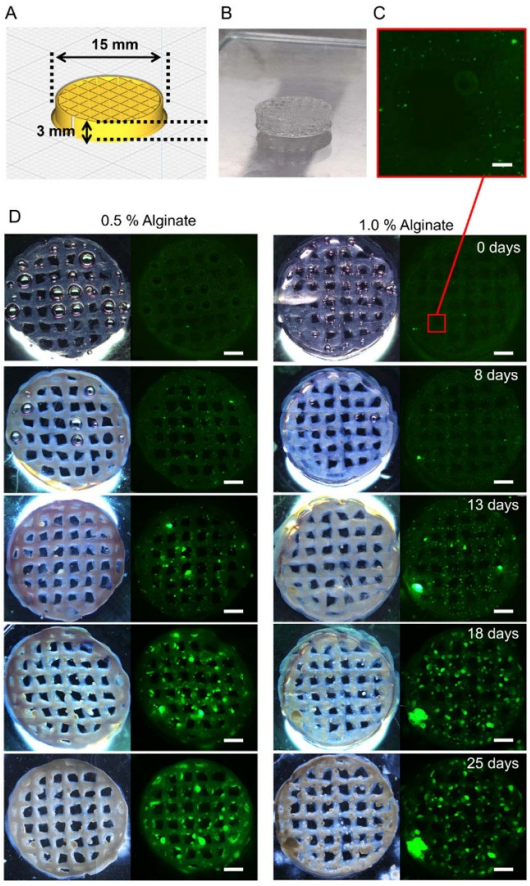

Figure 8. Cellular growth in 3D-bioprinted cylinders (3 mm height, 15 mm diameter, grid infill line width: ∼400–500 µm). Cells: HuH7^{EGFP} cells (expressing GFP). (A) Scheme of the sample geometry and dimensions, and (B) Representative printed sample post-printing. (C) Representative close-up image demonstrating cellular presence. (D) Bright field and fluorescent stereo-microscope images tracking cellular growth over 25 d (cell seeding density was 50 000 cells ml^{-1}). The hydrogel composition was 14% gelatin and 0.5% alginate (left, printed at 30 °C) or 1.0% alginate (right, printed at 31 °C). The print duration per sample was ∼10 min. Scale bar: C: 100 µm, D: 1 mm. For each sample, two pictures were taken with 8x magnification, which were then stitched using the software FIJI.

Fluorescence microscopy observations post-printing confirmed cells to be present throughout the printed samples. After eight days of cultivation, the emergence of aggregates became evident through the increased presence of fluorescent clusters, especially for the hydrogel with 0.5 wt.% alginate. By day 13, robust growth was evident, with distinct cell aggregates visible under both fluorescence and brightfield microscopy. As cultivation progressed, the size of the aggregates increased for both hydrogel types. These results demonstrate that cells not only survive the bioprinting process but also actively proliferate within the bioprinted hydrogel structure. Throughout the cultivation period, inhomogeneities in cellular distribution, characterized by bright spots, became apparent, suggesting areas of higher cellular density, possibly indicating inefficiencies in hydrogel-cell mixing. This aligns well with the growth patterns observed in stamped cell-laden hydrogels (figure 7(A)). The mixing method employed in this study—where cells are pipetted into the hydrogel and gently stirred with a spatula—represents the state-of-the-art procedure in the field of bioprinting. While more vigorous stirring could potentially improve cell homogeneity, it introduces three significant challenges: (i) increased shear forces that can compromise cell membrane integrity and reduce cellular viability, (ii) the introduction of air bubbles into the bioink, which can lead to extrusion issues as the bioink becomes 'compressible,' resulting in faulty extrusion behavior, and (iii) disruption of the bioink's rheological properties due to mechanical stress, rendering it unprintable. Given these limitations, a straightforward solution to the issue of inhomogeneous cell distribution remains elusive. Of note, the samples exhibited increased fragility throughout cultivation. This may be attributed to a melting of the gelatin at 37 °C (the standard cell culture incubator temperature) and the gradual solubilisation of alginate during cultivation due to its non-permanent cross-linking with Ca^{2+} ions. As calcium ions diffuse out into the surrounding medium, the ionic cross-links weaken, leading to a loss of structural integrity. Over time, both components are progressively removed during medium exchanges [31, 51–54]. Moreover, the presence of cell clusters within the channel network implies a positive correlation between proximity to the infill grid and cellular proliferation, likely due to optimized nutrient and oxygen exchange and reduced metabolite buildup.

Collectively, by customizing a standard FDM printer and developing the PQI method to optimize slicer settings for our specific hydrogel formulations, we achieved precise 3D constructs that effectively support liver cell growth. The PQI method could serve as an effective tool for optimizing the printability of various bioinks—especially naturally derived polymers like fibrin, Matrigel, and collagen, which are commonly used in bioprinting. However, adapting our system to accommodate these materials may require further modifications to the extruder. Commercial systems based on syringe-based extrusion, such as the Matribot (Corning, USA), have demonstrated compatibility with these bioinks. Our system is expected to be particularly well-suited for fibrin bioprinting, as this material can be printed at 24 °C–32 °C and reinforced with additives like gelatin and alginate to enhance mechanical properties and shape fidelity [55, 56]. In contrast, since both Matrigel and collagen require extrusion at low temperatures, modifying our system to include a cooling system instead of a heating cartridge would be necessary to maintain optimal print conditions. These bioinks, which are typically printed at 4 °C to

prevent premature polymerization, often suffer from low print quality under these conditions [57, 58]. However, their printability can be improved by incorporating additives, such as alginate [59, 60]. In this context, the PQI method could be useful to enhance print quality.

Conventional bioprinting technologies often face challenges related to low printing resolution and dimensional inaccuracies, making it difficult to replicate complex tissue structures such as liver or kidney models [26]. Our approach overcomes these limitations by producing structures with well-defined, highly accurate, and reproducible geometries, representing a significant advancement in bioprinting technology for fabricating complex tissues. We hypothesize that our system is capable of printing any structure, provided the achieved resolution meets the complexity requirements of the intended tissue. The cultivation of large complex tissue structures requires dynamic culture systems, such as perfusion bioreactors, to ensure adequate nutrient and oxygen supply. The high geometric fidelity of our bioprinted structures enables computational fluid dynamics (CFD) analysis to predict shear forces exerted by medium flow and identify potential dead zones—regions with inadequate nutrient and oxygen diffusion—before fabrication. By simulating these parameters prior to printing, CFD analysis facilitates the optimization of scaffold geometry, ensuring uniform flow distribution and eliminating critical deficiencies. However, this approach relies on the high precision of the bioprinted structure to accurately translate CFD predictions into functional designs. This iterative process can enhance the performance of bioprinted structures, ultimately increasing the likelihood of successful *in vitro* tissue development. The developed system could be further engineered to accommodate multiple print heads or hybrid manufacturing techniques, enabling the fabrication of hierarchical structures (e.g. large blood vessels), which are of significant scientific interest. These structures more closely mimic the native cellular environment, improving biocompatibility and increasing the likelihood of successful implantation [61]. Altogether, our results underscore the potential of the PQI method, combined with the repurposing of low-cost FDM printers, to enable functional bioprinting applications, making high-precision bioprinting more accessible and scalable.

3. Conclusions

This work introduces a cost-effective transformation of a standard off-the-shelf FDM printer into a fully functional bioprinter for alginate/gelatin-based bioinks, offering a compact design that can operate easily within a biosafety cabinet. By ensuring sterility through autoclavable components—especially those components that come into direct contact with cells—and UV-sanitized hardware, we maintain aseptic conditions critical for cell-based experiments. The integration of a thermostated extruder with an adjustable nozzle temperature facilitates the extrusion of molten gelatin-based bioinks, reducing viscosity and minimizing shear forces, resulting in improved cell viability during the printing process. Not only did the cells survive the bioprinting process, but they also proliferated over several weeks, demonstrating the system's effectiveness for cell-based applications. This thermostated extruder is anticipated to allow compatibility with various thermosensitive bioinks, greatly expanding the printer's utility in bioprinting. We postulate that the introduced modifications can be retrofitted to any FDM printer with sufficient space to accommodate the customized extruder.

Most importantly, we demonstrate that one of the fundamental challenges of FDM-based bioprinting—optimizing slicer parameters for a given bioink—can be effectively addressed using the developed PQI method. This method provides a quantitative measure of print quality through simple two-layer grid structures, enabling the precise adjustment of slicer parameters to align bioink composition with optimal printing performance. These adjustments can then be transferred to more complex structures, as demonstrated in this study. As a result, the PQI method offers a streamlined approach to optimizing slicer settings, ensuring consistent, high-quality bioprints tailored to specific experimental needs, without requiring the use of rheological measurements. This is expected to simplify the bioprinting process by bridging the gap between bioink composition and ideal printing parameters. In our case study, applying the PQI method to an alginate/gelatin blend resulted in two key outcomes: superior print quality and enhanced cellular proliferation. We propose that the PQI method could serve as an effective solution to the current lack of a universally accepted printing benchmark—common in standard FDM printing—while helping researchers using 3D-bioprinting technology to improve print quality more straightforwardly. However, while the PQI method could serve as an initial print quality benchmark for the x and y dimensions in bioprinting, further refinement will be needed to extend its application to the z-dimension, fully unlocking its potential.

To the best of our knowledge, this is the first comprehensive study that covers the full bioprinting pipeline—from the modification of the bioprinter and optimization of slicer settings to long-term cell culture. This adaptable and cost-effective solution brings sophisticated bioprinting technology within reach of research groups with limited resources, paving the way for significant advancements in 3D cell culture and tissue engineering. The newly developed PQI method is expected to help solving some of the challenges of the bioprinting field by providing a

standardized, reliable approach to optimizing print quality across diverse bioinks and printer systems, ultimately facilitating reproducibility and scalability in tissue engineering applications.

4. Materials and methods

4.1. Materials

If not otherwise indicated, cell culture materials were from Greiner Bio-One International GmbH (Frickenhausen, Germany). Chemicals were from Sigma-Aldrich (Taufkirchen, Germany). Linear PEI (l-PEI, 25 kDa) was from Polysciences (Polysciences Europe GmbH, Eppenheim, Germany). L-glutamine, penicillin, streptomycin, Dulbecco's Phosphate-Buffered Saline without Ca^{2+} and Mg^{2+} (DPBS), Dulbecco's modified Eagle's medium (DMEM, without phenol red), trypsin were from Lonza (Lonza Group Ltd, Basel, Switzerland). Opti-MEM culture medium supplemented with GlutaMAX was from ThermoFisher Scientific (Dreieich, Germany). Fetal calf serum (FCS) was from Sigma Aldrich (Taufkirchen, Germany). Trypan blue was from VWR Life Science (Darmstadt, Germany). Neomycin G418 solution was from Carl Roth (Karlsruhe, Germany). pEGFP-N1 (4.7 kb) plasmid, encoding for the EGFP driven by the cytomegalovirus (CMV) immediate early promoter, was from Clontech (Mountain View, CA). Sodium-alginate (ordering number: B25266.36, lot: 10234325) was purchased from ThermoFisher Scientific (Dreieich, Germany). Gelatin from porcine skin (300 g bloom, ordering number: SIALG1890-100, lot: SLCG4328) was from Sigma-Aldrich (Taufkirchen, Germany). The original FDM printer was an Anet A8 Plus, purchased at a local hardware store. Glass syringes (2 and 5 ml) were from Fortuna Optima, Poulten & Graf GmbH, Mannheim, Germany.

4.2. Mechanical design and construction

The 3D models (figure 2) of the extruder designs were made with Fusion360 (version 2.0.19966 x86_64, Autodesk Inc., USA). 3D printed plastic parts were manufactured using an Ender 3 3D printer (Creality, China) with either autoclavable 'Greentec Pro' filament purchased from Extrudr (FD3D GmbH, Austria), generic PLA or TPU filament (both from Prima Printer Nordic AB, Sweden). The slicing program Cura (V. 5.3.1, Ultimaker B.V, Netherlands) was used for all plastic and bioprinted parts to turn the geometric .stl files into Gcode, for the respective printer to execute. The recommended slicer settings were used when printing these materials. Metal parts were fabricated by the University of Bayreuth workshop. A complete parts list (Tables S1-S3) and detailed assembly instructions (figures S4–S11) can be found in the SI. The necessary construction files (i.e. step and stl files) for replicating this machine are available as supplementary materials on the publisher's website.

4.3. Cell and culture conditions

Cells were maintained in a standard cell culture incubator (5.0% CO_2, 37 °C, 95% humidity). HuH7 (hepatocellular carcinoma cell line generously gifted by Dr Di Fazio, Marburg, Germany) and $HuH7^{EGFP}$ cells were maintained in DMEM supplemented with 10% FCS, 2 mM L-glutamine, 100 units ml^{-1} penicillin, and 100 µg ml^{-1} streptomycin, 1x Amphotericin B. The cells were passaged every 2–3 d by trypsinization. The cell-laden stamped hydrogels and bioprinted constructs were kept in the same culture medium and conditions in appropriately sized well plates. In all cases, the culture medium was replaced every 2–3 d to replenish nutrients and remove metabolites.

4.4. Establishment of the $HuH7^{EGFP}$ cell line

The pEGFP-N1 expression plasmid containing a selectable marker (NeoR) was stably transfected into HuH7 cells using l-PEI according to a protocol developed in our group [62]. Transfected cells were then selected with G418 (500–800 µg ml^{-1}). The selective medium was replaced every 2–3 d until non-transfected cells were no longer viable. Resistant clones were visible within 2–3 weeks cultivation. Thereafter, cells expressing a high level of EGPF were sorted ('high producer bulk fraction') using a cell sorter equipped with two lasers (488 and 561 nm) (S3e cell sorter, BioRad, Feldkirchen, Germany) and individual clones were subsequently isolated by two-rounds of conventional limiting dilution method. Briefly, clones were isolated into separate wells of a 96-well plate containing growth medium supplemented with G418. The level of EGFP expression was evaluated by flow cytometry equipped with three lasers (405, 488, and 635 nm) (FC500, Beckman Coulter, Krefeld, Germany). One clone expressing a high level of EGFP was identified and further expanded to larger culture vessels. Long-term EGFP expression in the stable clone was validated by monitoring fluorescence intensity over multiple passages. This clone was used for the stamped hydrogels and the bioprinting experiments. The EGFP protein, expressed in the cytoplasm, is released from cells when the cell membrane is compromised. This provides an indirect assessment of cell viability: healthy cells with intact membranes exhibit green fluorescence, while damaged cells lose fluorescence as EGFP leaks out. The fluorescence of the cells enabled the estimation of cellular health using fluorescence microscopy, facilitating the evaluation of 3D bioprinted constructs.

4.5. Hydrogels and bioink preparation

Hydrogels used in this work were based on sodium alginate and gelatin. Sodium-alginate and gelatin in

the form of dry powders were first sterilized in thin layer via UV-radiation (UV-C box medium, Purion GmbH, Germany) for five cycles of 2 min in specially in-house designed shells to ensure homogeneous UV exposure while minimizing the damage to the hydrogel reported to be caused by UV treatment [25, 44]. The shells were printed with PLA. Sterile alginate and gelatin powder were then dissolved overnight in sterile DPBS in reaction tubes held at 45 °C in a water bath. Potential bubbles in the hydrogel were removed by centrifuging the molten hydrogel at 1000 *g* for 5 min. If not stated otherwise, hydrogels used in this work were made with 14 wt. % gelatin and 2 wt. % alginate. The composition of the hydrogel is always given in % (w/v).

To prepare bioink, the adherent HuH7^{EGFP} cells were collected from the culture dish by trypsinization. The trypsin was inactivated using culture medium, and the cells were counted using trypan blue exclusion assays following standard laboratory protocols. The required living cells quantity was subsequently collected by centrifugation at 200 *g* for 5 min. After discarding the supernatant, the cells were directly resuspended in 50 µl of DPBS without additional washing steps. The resuspended cells were gently pipetted into the hydrogel (cell concentration in the bioink: 5×10^4 cells ml^{-1}), which was cooled down to the printing temperature in the syringe before cell addition, followed by a quick gentle stirring (e.g. using a sterile spatula) to ensure an even distribution of the cells within the hydrogel while maintaining strict aseptic conditions. Importantly, the vessel was not maintained in a temperature-controlled environment when cells were added to the hydrogel to create the bioink. Subsequently, the cell-laden hydrogel was transferred into the syringe and immediately placed into the pre-warmed extruder (see below).

The stamped hydrogels were prepared with a specially designed tool (figure S3). In short, the autoclavable device produced flat master molded hydrogel 0.5 mm in height. A cellular density of 9×10^4 cells ml^{-1} hydrogel, resulting in around 2000 cells/stamped hydrogel, was used. After crosslinking with sterile 0.1 M $CaCl_2$, for 3 min, a sterile punch was used to stamp cylinders out of the master film. These cylinders of 7.5 mm diameter were transferred into a standard 24-well plate using sterile spatulas. The samples were cultivated, as previously stated.

4.6. Bioprinting and post-processing

The bioprinter was operated within a biosafety cabinet (Waldner Electronics, Germany). Before UV sterilization, the bioprinter's electronics bay and plastic parts were covered with aluminum tape to protect the electronic components and provide a clean surface. The extruder (consisting of the aluminum heat block, the glass syringe, the TPU surface cushion, and its holder) and spare materials for bioprinter operation were autoclaved. Prior to bioprinting, the Gcode was transferred to the bioprinter via an SD card. The bioprinting settings are provided with the slicer profile and in table 1. The slicer settings were fine-tuned from the default 0.4 mm nozzle and 0.2 mm layer height profile, referred to as the 'Baseline Profile,' specifically designed for printing PLA (table S7). The settings were developed with hydrogel consisting of 0–20 wt.% gelatin and 0–10 wt.% alginate. A 27 G needle was used as the nozzle (Ø: 0.21 mm). The file containing the optimized settings (file name: Slicer_Settings_Bioprinter.curaprofile) can be downloaded from the publisher webpage as a printer profile for Ultimaker's Cura Slicing software for an Anet A8 Plus printer. In the slicer, the Gcode '*M302 P1;*' was added as Start-Gcode to allow cold extrusion, otherwise blocked by the printer's firmware.

Under aseptic conditions, the pre-warmed glass syringe was filled with the prepared bioink to about 50% of its total capacity without introducing bubbles, and a 27 G needle (nominal internal diameter: 0.21 mm, Blunt tip, Braun, Germany) was installed as the nozzle. The extruder was pre-warmed by setting the printing temperature on the machine's console to avoid accidental polymerization when installing the syringe. The syringe with bioink was installed in the pre-warmed extruder, and the bioink was given time to equilibrate at the printing temperature before the print was started using the printer's console. Post-printing, the bioprinted construct was crosslinked by submersion on the print bed in sterile 0.1 M $CaCl_2$ solution for 3 min. After crosslinking, the printed object popped off the print bed and was transferred into an appropriate tissue culture plate using a sterile spatula. The cell-laden samples were then cultivated, as stated above.

To assess cellular viability postprint, single-layer lines (length: 10 mm) were printed onto microscope slides using bioink with a cellular load of 2×10^6 cells ml^{-1}. HuH7^{EGFP} cells were used as previously. Dead cells within the hydrogel were counterstained with propidium iodide (1 µg ml^{-1}), which was applied after washing the samples with DPBS. The samples were incubated at 37 °C, 95% relative humidity, and 5% CO_2 for 15 min, shielded from light with aluminum foil. After incubation, the staining solution was removed, and the samples were washed three times with DPBS. The samples were subsequently analyzed using an epifluorescence microscope. Dead cells fluoresced red, while living cells were green due to stable GFP expression. Cellular viability was calculated as the ratio between living cells and the total cell count. Control samples were prepared by carefully placing bioink onto a microscope slide using a spatula and treating them in the same manner.

The printed constructs and the cellular behavior were analyzed with stereo-microscopy (SMZ 745 T, Nikon, Japan), light microscopy (PrimoVert, Zeiss AG, Germany), and fluorescence microscopy (M205 FCA, Leica, Germany & Olympus BX51, Japan).

4.7. PQI calculation

The PQI was derived by printing two-layer grids (20 mm × 17 mm, grid line distance: 1 mm, hydrogel composed of 0.5–2.0 wt. % alginate and 14 wt. % gelatin, slicer settings displayed in table 1, 'Settings III ') and evaluating the interconnecting channels geometries in FIJI (V. 1.53 t). Equations (1)–(4) were used to calculate PQI. The perimeter and area required for the calculation are calculated automatically by tracing and measuring the hole in FIJI. A schematic for the calculation is presented in figure 5.

The square ratio was calculated according to equation (1):

$$\text{Square Ratio(SR)} = \frac{a}{b} \tag{1}$$

with a: distance between the parallel bottom layer lines, measured at the cross-section, and b: distance between the parallel top layer lines, measured at the cross-section.

The width ratio was calculated according to equation (2):

$$\text{Width Ratio(WR)} = \frac{a}{c} \tag{2}$$

with a: distance between the parallel bottom layer lines, measured at the cross-section, and c: distance between the parallel top layer lines, measured at the top lines' centers.

The squareness ratio was calculated according to equation (3):

$$\text{SQuareness}(SQ) = \frac{Perimeter^2}{16 * A} \tag{3}$$

with A: traced area of interconnected channels and Perimeter: traced perimeter of the interconnected channels.

The PQI was calculated according to equation (4):

$$\text{Print Quality Index(PQI)} = \sqrt{(1-\text{SR})^2 + (1-\text{WR})^2 + (1-\text{SQ})^2} \tag{4}$$

with SR: calculated square ratio, WR: calculated width ratio, and SQ: calculated squareness.

4.8. Cell proliferation assessment

Cellular aggregates within stamped hydrogels were imaged using brightfield microscopy (Primovert, Zeiss, Germany). Due to sample dimensions exceeding the camera's field of view, multiple images were captured per sample and subsequently stitched together using FIJI (V. 1.53 t) and the Grid/Collection plugin [63]. This image processing enabled precise measurement of cellular aggregate area and perimeter within the hydrogel. Circularity was calculated using equation (5), with area and perimeter automatically calculated by the software for the outlined regions,

$$Circularity = \frac{4\pi * Area}{Perimeter^2} \tag{5}$$

with Area: traced area of the cellular aggregates and Perimeter: traced perimeter of the cellular aggregates.

4.9. Statistical evaluation

Group data are reported as mean ± standard error of the mean. If not otherwise stated, n represents the number of independent experiments. OriginPro software (version 2022, OriginLab, USA) was used for one-way and two-way ANOVA with Bonferroni multiple comparison tests to determine whether data groups differed significantly. Statistical significance was defined as $^{*}p \leqslant 0.05$, $^{**}p \leqslant 0.01$, $^{***}p \leqslant 0.001$.

Data availability statement

All data that support the findings of this study are included within the article (and any supplementary files).

CRediT authorship contribution statement

Conceptualization, L.M., V.J. and R.F.; Experimental part, L.M.; data analysis, L.M., and V.J.; writing original draft preparation, L.M.; writing/review and editing, V.J., R.F. All authors provided critical feedback and helped to shape the research, analysis, and the resulting manuscript. All authors have read and agreed to the published version of the manuscript.

Funding note

Open Access funding enabled and organized by Projekt DEAL.

Acknowledgment

We thank Professor A. Möglich (Department of Biochemistry, University of Bayreuth) for providing access to the cell sorter and Professor Heike Feldhaar for access to the fluorescence microscope.

Conflict of interest

The authors declare no conflict of interest.

ORCID iDs

Leif O Meyer https://orcid.org/0000-0002-0172-4604
Valérie Jérôme https://orcid.org/0000-0001-6492-2168
Ruth Freitag https://orcid.org/0000-0002-6569-9137

References

[1] Sun W *et al* 2020 The bioprinting roadmap *Biofabrication* **12** 22002
[2] Vijayavenkataraman S, Yan W-C, Lu W F, Wang C-H and Fuh J Y H 2018 3D bioprinting of tissues and organs for regenerative medicine *Adv. Drug Deliv. Rev.* **132** 296–332
[3] Bedir T, Ulag S, Ustundag C B and Gunduz O 2020 3D bioprinting applications in neural tissue engineering for spinal cord injury repair *Mater. Sci. Eng. C* **110** 110741
[4] Wan Z, Zhang P, Liu Y, Lv L and Zhou Y 2020 Four-dimensional bioprinting: current developments and applications in bone tissue engineering *Acta Biomater.* **101** 26–42
[5] Nesic D, Durual S, Marger L, Mekki M, Sailer I and Scherrer S S 2020 Could 3D printing be the future for oral soft tissue regeneration? *Bioprinting* **20** e00100
[6] Agarwal T *et al* 2021 Recent advances in bioprinting technologies for engineering hepatic tissue *Mater. Sci. Eng. C* **123** 112013
[7] Liu N *et al* 2021 Advances in 3D bioprinting technology for cardiac tissue engineering and regeneration *Bioact. Mater.* **6** 1388–401
[8] Choudhury D, Anand S and Naing M W 2018 The arrival of commercial bioprinters—Towards 3D bioprinting revolution! *Int. J. Bioprint.* **4** 139
[9] Liu W, Zhong Z, Hu N, Zhou Y, Maggio L, Miri A K, Fragasso A, Jin X, Khademhosseini A and Zhang Y S 2018 Coaxial extrusion bioprinting of 3D microfibrous constructs with cell-favorable gelatin methacryloyl microenvironments *Biofabrication* **10** 24102
[10] Zhang Z, Wu C, Dai C, Shi Q, Fang G, Xie D, Zhao X, Liu Y-J, Wang C C L and Wang X-J 2022 A multi-axis robot-based bioprinting system supporting natural cell function preservation and cardiac tissue fabrication *Bioact. Mater.* **18** 138–50
[11] Bharadwaj T and Verma D 2021 Open source bioprinters: revolutionizing the accessibility of biofabrication *Bioprinting* **23** e00155
[12] Engberg A, Stelzl C, Eriksson O, O'Callaghan P and Kreuger J 2021 An open source extrusion bioprinter based on the E3D motion system and tool changer to enable FRESH and multimaterial bioprinting *Sci. Rep.* **11** 21547
[13] Budde L, Ihler S, Spindeldreier S, Lücking T, Meyer T, Bodenschatz E and Zimmermann W H 2022 A six degree of freedom extrusion bioprinter *Curr. Dir. Biomed. Eng.* **8** 137–40
[14] Pagan E *et al* 2023 A handheld bioprinter for multi-material printing of complex constructs *Biofabrication* **15** 035012
[15] You S *et al* 2023 High cell density and high-resolution 3D bioprinting for fabricating vascularized tissues *Sci. Adv.* **9** eade7923
[16] Horvath J and Cameron R 2020 Mastering 3D printing *A Guide to Modeling, Printing, and Prototyping* (Apress) (https://doi.org/10.1007/978-1-4842-5842-2)
[17] Koch F, Thaden O, Tröndle K, Zengerle R, Zimmermann S and Koltay P 2021 Open-source hybrid 3D-bioprinter for simultaneous printing of thermoplastics and hydrogels *HardwareX* **10** e00230
[18] Tashman J W, Shiwarski D J and Feinberg A W 2022 Development of a high-performance open-source 3D bioprinter *Sci. Rep.* **12** 22652
[19] Kahl M, Gertig M, Hoyer P, Friedrich O and Gilbert D F 2019 Ultra-low-cost 3D bioprinting: modification and application of an off-the-shelf desktop 3D-printer for biofabrication *Front. Bioeng. Biotechnol.* **7** 184
[20] Garciamendez-Mijares C E *et al* 2023 Development of an affordable extrusion 3D bioprinter equipped with a temperature-controlled printhead *Int. J. Bioprint.* **9** 244
[21] Shin J, Chung H, Kumar H, Meadows K, Park S, Chun J and Kim K 2024 3D bioprinting of human iPSC-Derived kidney organoids using a low-cost, high-throughput customizable 3D bioprinting system *Bioprinting* **38** e00337
[22] Woods P, Smith C, Clark S and Habib A 2024 Integrating pneumatic and thermal control in 3D bioprinting for improved bio-ink handling *Designs* **8** 83
[23] Dharmaraj J J J, Navasingh R J H, Krolczyk G and Pitchumani S V 2024 Extrusion-based bioprinting in a cost-effective bioprinter *Machines* **12** 518
[24] Pakhomova C, Popov D, Maltsev E, Akhatov I and Pasko A 2020 Software for Bioprinting *Int. J. Bioprint.* **6** 279
[25] Lorson T, Ruopp M, Nadernezhad A, Eiber J, Vogel U, Jungst T and Lühmann T 2020 Sterilization methods and their influence on physicochemical properties and bioprinting of alginate as a bioink component *ACS Omega* **5** 6481–6
[26] Guida L, Cavallaro M and Levi M 2024 Advancements in high-resolution 3D bioprinting: exploring technological trends, bioinks and achieved resolutions *Bioprinting* **44** e00376
[27] Boularaoui S, Al Hussein G, Khan K A, Christoforou N and Stefanini C. 2020 An overview of extrusion-based bioprinting with a focus on induced shear stress and its effect on cell viability *Bioprinting* **20** e00093
[28] Sánchez-Sánchez R, Rodríguez-Rego J M, Macías-García A, Mendoza-Cerezo L and Díaz-Parralejo A 2023 Relationship between shear-thinning rheological properties of bioinks and bioprinting parameters *Int. J. Bioprint.* **9** 687
[29] Çelik E, Bayram C, Akçapınar R, Türk M and Denkbaş E B 2016 The effect of calcium chloride concentration on alginate/Fmoc-diphenylalanine hydrogel networks *Mater. Sci. Eng. C* **66** 221–9
[30] Wang X, Ao Q, Tian X, Fan J, Tong H, Hou W and Bai S 2017 Gelatin-based hydrogels for organ 3D bioprinting *Polymers* **9** 401
[31] Mondal A, Gebeyehu A, Miranda M, Bahadur D, Patel N, Ramakrishnan S, Rishi A K and Singh M 2019 Characterization and printability of Sodium alginate -Gelatin hydrogel for bioprinting NSCLC co-culture *Sci. Rep.* **9** 19914
[32] Ouyang L, Yao R, Zhao Y and Sun W 2016 Effect of bioink properties on printability and cell viability for 3D bioplotting of embryonic stem cells *Biofabrication* **8** 35020
[33] He Y, Yang F, Zhao H, Gao Q, Xia B and Fu J 2016 Research on the printability of hydrogels in 3D bioprinting *Sci. Rep.* **6** 29977
[34] Zhang Y, O'Mahony A, He Y and Barber T 2024 Hydrodynamic shear stress' impact on mammalian cell properties and its applications in 3D bioprinting *Biofabrication* **16** 022003
[35] Mohammadrezaei D, Podina L, De Silva J and Kohandel M 2024 Cell viability prediction and optimization in extrusion-based bioprinting via neural network-based Bayesian optimization models *Biofabrication* **16** 025016
[36] Tarassoli S P, Jessop Z M, Jovic T, Hawkins K and Whitaker I S 2021 Candidate bioinks for extrusion 3D bioprinting-A systematic review of the literature *Front. Bioeng. Biotechnol.* **9** 616753
[37] Łabowska M B, Cierluk K, Jankowska A M, Kulbacka J, Detyna J and Michalak I 2021 A review on the adaption of alginate-gelatin hydrogels for 3D cultures and bioprinting *Materials* **14** 858

[38] Gregory T, Benhal P, Scutte A, Quashie D, Harrison K, Cargill C, Grandison S, Savitsky M J, Ramakrishnan S and Ali J 2022 Rheological characterization of cell-laden alginate-gelatin hydrogels for 3D biofabrication *J. Mech. Behav. Biomed. Mater.* **136** 105474
[39] Jin Y, Yang T, Ju S, Zhang H, Choi TY and Neogi A 2020 Thermally tunable dynamic and static elastic properties of hydrogel due to volumetric phase transition *Polymers* **12** 1462
[40] Schmidt S K, Schmid R, Arkudas A, Kengelbach-Weigand A and Bosserhoff A K 2019 Tumor cells develop defined cellular phenotypes after 3D-bioprinting in different bioinks *Cells* **8** 1295
[41] Li Y and Kumacheva E 2018 Hydrogel microenvironments for cancer spheroid growth and drug screening *Sci. Adv.* **4** eaas8998
[42] Wang C, Tong X and Yang F 2014 Bioengineered 3D brain tumor model to elucidate the effects of matrix stiffness on glioblastoma cell behavior using PEG-based hydrogels *Mol. Pharm.* **11** 2115–25
[43] Cavo M, Fato M, Peñuela L, Beltrame F, Raiteri R and Scaglione S 2016 Microenvironment complexity and matrix stiffness regulate breast cancer cell activity in a 3D *in vitro* model *Sci. Rep.* **6** 35367
[44] Carranza T, Zalba-Balda M, Jose Barriola B B M, de la Caba K and Guerrero P 2022 Effect of sterilization processes on alginate/gelatin inks for three-dimensional printing *Int. J. Bioprint.* **9** 645
[45] Cao N, Chen X B and Schreyer D J 2012 Influence of calcium ions on cell survival and proliferation in the context of an alginate hydrogel *ISRN Chem. Eng.* **2012** 1–9
[46] Singh S K, Abbas S, Saxena A K, Tiwari S, Sharma L K and Tiwari M 2020 Critical role of three-dimensional tumorsphere size on experimental outcome *Biotechniques* **69** 333–8
[47] Ruoß M, Rebholz S, Weimer M, Grom-Baumgarten C, Athanasopulu K, Kemkemer R, Käß H, Ehnert S and Nussler A K 2020 Development of scaffolds with adjusted stiffness for mimicking disease-related alterations of liver rigidity *J. Funct. Biomater.* **11** 17
[48] Desai S S, Tung J C, Zhou V X, Grenert J P, Malato Y, Rezvani M, Español-Suñer R, Willenbring H, Weaver V M and Chang T T 2016 Physiological ranges of matrix rigidity modulate primary mouse hepatocyte function in part through hepatocyte nuclear factor 4 alpha *Hepatology* **64** 261–75
[49] Xu H-Q, Liu J-C, Zhang Z-Y and Xu C-X 2022 A review on cell damage, viability, and functionality during 3D bioprinting *Mil. Med. Res.* **9** 70
[50] Jain T, Baker H B, Gipsov A, Fisher JP, Joy A, Kaplan DS and Isayeva I 2021 Impact of cell density on the bioprinting of gelatin methacrylate (GelMA) bioinks *Bioprinting* **22** e00131
[51] Hu T and Lo A C Y 2021 Collagen-alginate composite hydrogel: application in tissue engineering and biomedical sciences *Polymers* **13** 1852
[52] Andersen T, Auk-Emblem P and Dornish M 2015 3D Cell Culture in Alginate Hydrogels *Microarrays* **4** 133–61
[53] Soliman B G *et al* 2023 Programming delayed dissolution into sacrificial bioinks for dynamic temporal control of architecture within 3D-bioprinted constructs *Adv. Funct. Mater.* **33** 2210521
[54] Wu Z, Su X, Xu Y, Kong B, Sun W and Mi S 2016 Bioprinting three-dimensional cell-laden tissue constructs with controllable degradation *Sci. Rep.* **6** 24474
[55] Shpichka A *et al* 2020 Fibrin-based bioinks: new tricks from an old dog *Int. J. Bioprint.* **6** 269
[56] Terpstra M L *et al* 2022 Bioink with cartilage-derived extracellular matrix microfibers enables spatial control of vascular capillary formation in bioprinted constructs *Biofabrication* **14** 034104
[57] Alave Reyes-Furrer A *et al* 2021 Matrigel 3D bioprinting of contractile human skeletal muscle models recapitulating exercise and pharmacological responses *Commun. Biol.* **4** 1183
[58] Debnath S, Agrawal A, Jain N, Chatterjee K and Player D J 2025 Collagen as a bio-ink for 3D printing: a critical review *J. Mater. Chem. B* **13** 1890–919
[59] Jiao T, Lian Q, Lian W, Wang Y, Li D, Reis R L and Oliveira J M 2023 Properties of collagen/sodium alginate hydrogels for bioprinting of skin models *J. Bionic Eng.* **20** 105–18
[60] Northcutt L A, Questell A M, Rhoades J and Rafat M 2023 Development of an alginate-Matrigel hydrogel system to evaluate cancer cell behavior in the stiffness range of the bone marrow *Front. Biomater. Sci.* **2** 1140641
[61] Wang X, Liu X, Liu W, Liu Y, Li A, Qiu D, Zheng X and Gu Q 2023 3D bioprinting microgels to construct implantable vascular tissue *Cell Prolif.* **56** :e13456
[62] Schallon A, Synatschke C V, Jérôme V, Müller A H and Freitag R. 2012 Nanoparticulate nonviral agent for the effective delivery of pDNA and siRNA to differentiated cells and primary human T lymphocytes *Biomacromolecules* **13** 3463–74
[63] Preibisch S, Saalfeld S and Tomancak P 2009 Globally optimal stitching of tiled 3D microscopic image acquisitions *Bioinformatics* **25** 1463–5